Lappeenranta University of Technology
School of Engineering Science
Computational Engineering and Technical Physics

Abhiroop Chellu

OPTICAL PROPERTIES OF CLOSE-TO-SURFACE SELF-ASSEMBLED InAs/GaAs QUANTUM DOTS

Master's thesis

Examiners: Professor Erkki Lähderanta
Professor Bernardo Barbiellini

Supervisors: Dr. Teemu Hakkarainen
Professor Mircea Guina
Professor Erkki Lähderanta

ABSTRACT

Lappeenranta University of Technology
School of Engineering Science
Computational Engineering and Technical Physics

Abhiroop Chellu

OPTICAL PROPERTIES OF CLOSE-TO-SURFACE SELF-ASSEMBLED InAs/GaAs QUANTUM DOTS

Master's thesis

2018

49 pages, 35 figures, 3 tables, 62 references.

Examiners: Professor Erkki Lähderanta
Professor Bernardo Barbiellini

Supervisors: Dr. Teemu Hakkarainen
Professor Mircea Guina
Professor Erkki Lähderanta

Quantum dots are novel semiconductor nanostructures that show great potential to be the future of a wide range of nanoscale optoelectronic device applications like photodetectors, solar cells and lasers. Self-assembled InAs quantum dots (QDs) grown in a GaAs matrix are proposed to be the primary elements for single and entangled photon sources used in quantum cryptography and quantum information processing. In order to incorporate quantum dots into optoelectronic and nanophotonic applications, they need to be fabricated close to the device surface. Generally, a semiconductor-capping layer is overgrown on the quantum dots to stabilize them

and to minimize surface effects. The aim of this thesis is to investigate the influence of a GaAs capping layer on the optical properties of the InAs quantum dots.

The optical properties of single InAs/GaAs QDs are investigated as a function of their distance from the GaAs/air interface. Interaction between the zero-dimensional quantum dot states and surface states are studied in close-to-surface individual QDs having a well-defined electronic structure. Capping the QDs with an overgrown GaAs layer has significant effects on the structural and optical properties. The influence of a capping layer of different thicknesses, mainly on the optical properties of QDs, has been experimentally investigated using low-temperature photoluminescence spectroscopy, micro-photoluminescence spectroscopy and time-resolved photoluminescence spectroscopy. The QD photoluminescence (PL) and carrier lifetime measurements show that quantum tunneling effects result in a sharp reduction of photoluminescence efficiency and carrier lifetime with decreasing wetting-layer-surface distance. For distances less than 40 nm, broadening of the PL linewidths of single QDs was observed. Since the exciton recombination time and efficiency are the same as exhibited by QDs situated in the bulk, the most likely cause of the observed PL linewidth broadening is spectral diffusion or dephasing.

Acknowledgements

The work presented in this thesis was carried out at the Optoelectronics Research Centre (ORC) in Tampere University of Technology (TUT) during the spring of 2018. I would like to thank the Academy of Finland and the TUT Foundation for funding my research. I would like to acknowledge the support provided to me by Peter the Great St.Petersburg Polytechnic University (SPBPU) while taking part in the double degree program at Lappeenranta University of Technology (LUT). I would like to express my gratitude to the LUT foundation for funding my master's studies in Finland.

I must say, I have been quite lucky to take part in a unique study programme that allowed me to study and work in three universities. It might seem clichéd, but meeting people from around the world has been an interesting experience and I have taken great pleasure in learning about various cultures in different countries.

I would like to acknowledge my supervisor at SPBPU, Dr. Maxim Vinnichenko, for being patient and helpful. Dr. Mikhail Kurushkin is a wonderful person and has been a great friend. I greatly appreciate all the help he has provided me with during my stay in Russia.

I would like to express my gratitude to Prof. Mircea Guina, the current director of ORC, for providing me with the opportunity and total freedom to work in an excellent research environment. I am deeply grateful to Prof. Erkki Lähderanta, the head of the physics department at LUT, for motivating me to conduct my thesis research at ORC and for overseeing my studies at LUT.

I am grateful to all the people whom I have had the pleasure of working with at ORC. I would like to thank M.Sc. Eero Koivusalo for fabricating the quantum dot samples used for research in this thesis. I would especially like to thank my supervisor, Dr. Teemu Hakkarainen, for being a marvellous mentor during my thesis research. He has taken me under his wing and has shown, by example, what a good scientist (and a person) should be.

Lastly, but by no means the least, I would like to thank my family and my friends for their unwavering support and encouragement through thick and thin. It has been a challenging last few months for me, personally, and it would not have been possible to get through, most importantly, without my parents. They occupy an important place in my heart and I would love to dedicate this work to them.

Tampere, September 2018

Abhiroop Chellu

Table of Contents

Abstract **ii**

Acknowledgements **iv**

Table of Contents **vi**

List of Abbreviations **viii**

1 Introduction **1**

2 Self-assembled InAs/GaAs Quantum Dots 4

2.1 Introduction to molecular beam epitaxy 4

2.2 Pseudomorphic and Metamorphic growth modes 7

2.3 Stranski-Krastanow growth of InAs quantum dots 9

2.4 Effect of capping on the structural properties of quantum dots 11

2.5 Confined states and optical properties 13

3 Research Methodology **18**

3.1 Sample growth by molecular beam epitaxy 18

3.2 Scanning electron microscopy 22

3.3 Atomic force microscopy 24

3.4 Photoluminescence spectroscopy 26

3.5 Micro-photoluminescence spectroscopy and imaging 27

3.6 Time-resolved photoluminescence spectroscopy 29

4 Results and Discussions **31**

4.1 Results from SEM 31

4.2 Results from AFM 33

4.3 Results from low-temperature PL 35

4.4 Results from μ-PL 39

4.5 Results from TRPL 41

5 Conclusions 43

Bibliography 44

List of abbreviations

AlGaAs	Aluminium gallium arsenide
AFM	Atomic force microscopy
APD	Avalanche photodiode
BEP	Beam equivalent pressure
CCD	Charge-coupled device
DOS	Density of states
FSS	Fine-structure splitting
FVM	Frank-Van der Merwe growth mode
GaAs	Gallium arsenide
GR	Growth rate
InAs	Indium arsenide
LTPL	Low-temperature photoluminescence
MBE	Molecular beam epitaxy
MD	Misfit dislocation
ML	Monolayer
ORC	Optoelectronics Research Centre
PL	Photoluminescence
μ-PL	Micrometer scale photoluminescence
QD	Quantum dot
RHEED	Reflection high-energy electron diffraction
SAQD	Self-assembled quantum dot
SEM	Scanning electron microscopy

S-K	Stranski-Krastanow growth mode
STM	Scanning tunnelling microscopy
TCSPC	Time-correlated single photon counting
UHV	Ultra-high vacuum
V-W	Volmer-Weber growth mode
WL	Wetting layer

Chapter 1

1 Introduction

A crystalline material that is restricted in all the three spatial dimensions such that its electron and hole wave functions are confined within its volume is called a quantum dot (QD). Due to this confinement, termed as the "Quantum Confinement Effect", the energy levels of the charge carriers become quantized (figure 1.1). These quantization effects are more pronounced when the confining region's dimensions are comparable to the de Broglie wavelength (λ_{DB}) of the carriers.

$$\lambda_{DB} = \frac{h}{\sqrt{2mk_BT}}$$

where, h is Planck's constant, k_B is Boltzmann's constant, m is the effective mass of charge carriers inside the semiconductor and T is the absolute temperature. This results in the electronic and optical properties of quantum dots being dependent on their physical and structural properties at the nanoscale.

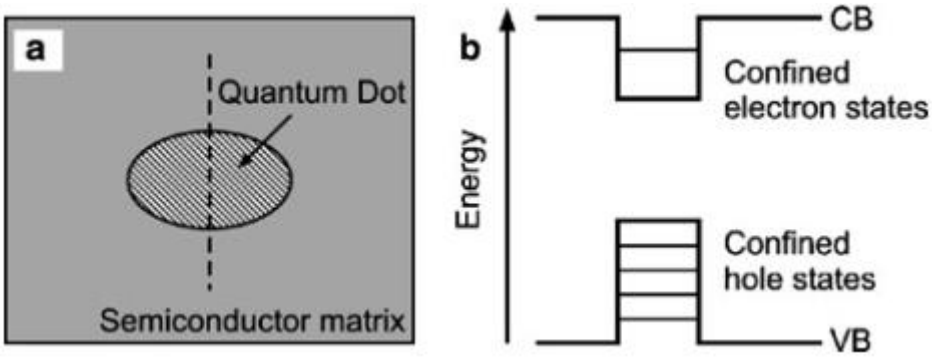

Figure 1.1. (a) An illustration of a QD in a semiconductor matrix. **(b)** A schematic of conduction and valence band at nanometric scales.

Semiconductor QDs are generally based on direct bandgap semiconductors, so that electronic transitions are direct both in real and in reciprocal space. They usually contain a few hundred

to a few thousand atoms. Although the size of a QD is much larger when compared to individual elemental atoms, they are often referred to as artificial atoms because they are still able to confine charge carriers in all three spatial dimensions. This three-dimensional confinement of charge carriers within a QD allows for a wide range of traditional optoelectronic applications, which include photodetectors [1], LEDs [2], Laser diodes [3] and solar cells [4], [5]. These applications are based on the fact that these discrete energy levels can be modified by tuning a QD's physical parameters such as shape, size, strain, and material composition.

Single-QD based devices have a single, localized/isolated quantum dot functioning as the active region that acts as a source for single photons and entangled photon pairs, with emission wavelengths ranging from the Ultraviolet to the Infrared. Single-QD devices promise a few distinctive advantages. For instance, the inhomogeneous or statistical broadening of the energy spectrum, which is inherent in the study and experimentation of QD ensembles, is largely minimized. Other obvious advantages include narrow and highly stable photoluminescence responses of isolated QDs, which make experimentation very convenient and efficient.

One of the most important applications of single-QD based devices is the generation of single, entangled and indistinguishable photons. Increasing interest in the fields of quantum cryptography [6] and quantum communications [7] over the last few decades has led to an unsurprisingly high amount of research into single-photon sources [8]. Single-photon sources are of paramount importance in numerous quantum information processing applications including linear optical quantum computing, quantum key distribution [6] and quantum memories [9]. Therefore, semiconductor quantum dots show great promise to be the forerunners of solid-state single-photon emitting devices [10]–[13].

A single-photon source generates photons that are distinguishable in time, that is, they are antibunched. Traditionally, single photons were generated by aggressively attenuating a strong light source. It is imperative to note the difference between an attenuated light source and a single-photon source - a laser may be designed to produce a single photon at any instant of time through attenuation, but it must be noted that the light produced still obeys classical statistics. Therefore, attenuated laser light will be contaminated with photon pairs and photon triplets. Quantum computing applications use photons that are governed by the rules of non-classical statistics. The ideal single-photon source produces completely deterministic light pulses of a well-defined polarization, on demand, and contains exactly one photon [14]. Incidentally, individual InAs QDs serve as an excellent source of single and entangled photons. Single InAs

QDs have been the topic of intense research in the recent past [15]–[17], which has revealed lot of details about their electrical and optical properties.

In order to implement single-QD devices for practical applications, the QDs must be grown close to the surface of the device. QDs grown close to the surface can be used in nanophotonic and nanoplasmonic applications. They also serve as an excellent platform to study experimental quantum cavity electrodynamics, which could help in understanding light-matter interactions at the nanoscale with unprecedented detail. Recently, there have been numerous reports on coupling QDs with optical cavity modes existing within microdisks [12], micropillars [18], [19] and photonic crystal microcavities [20], [21]. For implementing these designs practically, the QDs must be situated just tens of nanometers from the surface; under such conditions, the interaction between the QD and the surface states might cause degradation to the optical properties. This thesis carries out a systematic study of the optical properties of near-surface InAs/GaAs QDs situated at varying distances from the surface.

Chapter 2

2 Self-assembled InAs/GaAs quantum dots

2.1 Introduction to molecular beam epitaxy

Molecular beam epitaxy (MBE) is a very sophisticated technique suitable for growing thin layers made of metallic, semiconducting and insulating materials. J.R. Arthur and Alfred Y. Cho invented MBE at the Bell Telephone Laboratories in the late 1960s [22]. Epitaxial growth is the process in which atoms randomly deposited on the substrate rearrange themselves according to equilibrium configuration. There is precise crystal orientation between the epitaxial layers and the substrate. In MBE, epitaxial growth takes place layer-by-layer with atomic thickness and precision under ultra-high vacuum (UHV) conditions. The source materials for the films originate from elemental sources in the form of atomic or molecular beams. Atoms and molecules from different beams strike the substrate, where they are adsorbed onto the surface. Once on the surface, the atoms move around through surface diffusion until they reach a thermodynamically favorable location on the substrate. Because the surface diffusion of atoms requires considerable time, the quality of the film will be better with slower growth rates. Typically, the growth rate in MBE is 0.5-3 µm/h (1-3 monolayers). Inside the chamber, pressure varies in the range from 10^{-10} mbar, which is the typical value of pressure in an empty growth chamber, to 10^{-6} mbar, which is typically the pressure during the growth process. A UHV environment reduces the number of impure particles inside the MBE system, thus reducing unwanted adsorption of impurities on the growth surface. UHV also aids in maintaining collimation and direction of elemental beams of atoms and molecules that bombard the substrate in order to facilitate epitaxial growth. Additionally, depositing materials in the form of atomic or molecular beams ensures the growth of extremely sharp and abrupt interfaces between various layers. This feature is important for epitaxial growth of multiple quantum wells, nanowires, quantum dots and other related nanostructures [23]–[27].

As mentioned before, in an MBE system, beams of atoms or molecules of different elements are deposited on a heated base called a substrate. In this thesis, InAs/GaAs QDs are grown using MBE. The most important parameters of MBE growth are material fluxes and substrate temperature. Group III materials such as Al, Ga and In are injected from heated crucibles called as effusion cells. The most common type of effusion cell is the Knudsen effusion cell. The

material flux from these effusion cells is controlled by turning on and off mechanical shutters, whereas the temperature inside these cells determines the amount of material in the flux. Group V materials such as N, P, As and Sb are introduced into the system from crackers with needle valves. At low temperatures, quaternary molecules are introduced from the crackers, while at higher temperatures the molecules tend to be in the form of dimers. Section 4.1 gives a detailed explanation of the growth procedure followed in this thesis. Current MBE systems are accompanied by pre and post-growth in-situ analysis techniques. Due to the presence of relatively low residual gas on the surface and UHV conditions, analysis techniques like reflection high-energy diffraction (RHEED) and ellipsometry can be used during the growth process, in order to monitor and control the growth [28]. RHEED determines the growth rate (in ML/s) of the epitaxial layers [23], while ellipsometry provides information about surface roughness (or smoothness). The UHV environment also allows for post-growth analysis techniques such as Auger spectroscopy [29], to determine the composition of layers and scanning tunneling microscopy (STM) [30], [31], to study the surface topography in detail. Figure 2.1 illustrates the basic schematic of an MBE system.

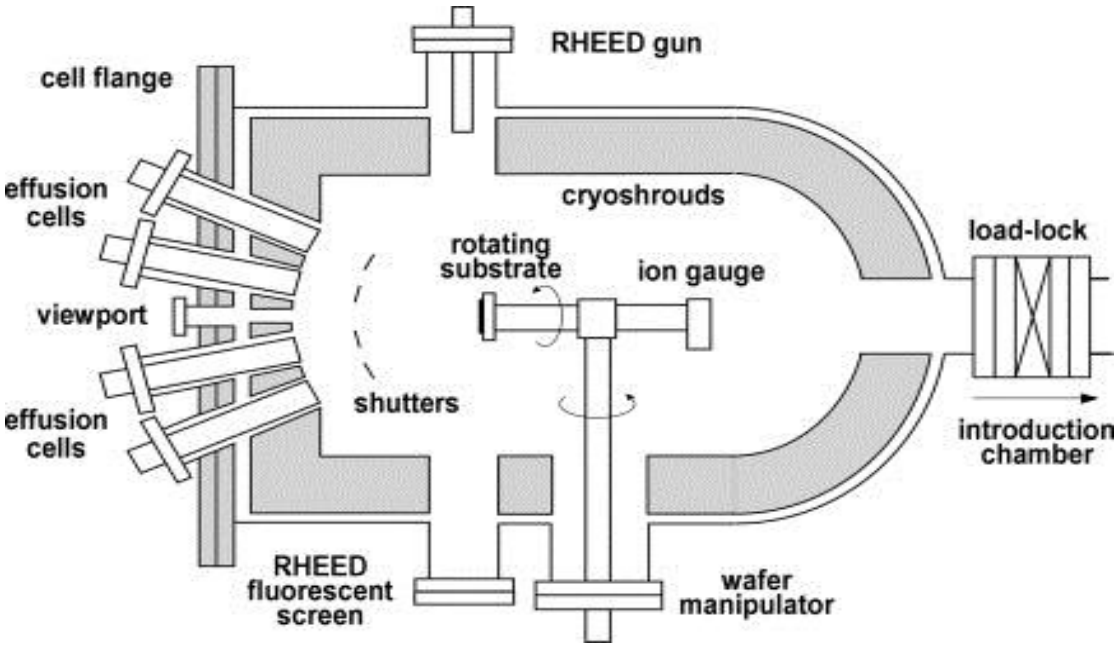

Figure 2.1. A basic schematic representation of an MBE system [25].

During MBE growth, the atomic or molecular source materials get physisorbed or chemisorbed to the substrate surface. On the surface, they may migrate to energetically favorable lattice sites, which is essential for the formation of an epitaxial layer. Notably, the thermodynamic behavior of the adatoms on the surface strongly depends on the material and the growth environment. In an MBE, epitaxial growth primarily takes place in three growth mechanisms: Frank-Van der Merve (FVM), Volmer-Weber (V-W) and Stranski-Krastanow (S-K) (shown in figure 2.2). In Frank-Van der Merve mode, the epitaxial growth takes place in two-dimensional layers, which is the most desirable to grow planar thin films. Volmer-Weber mode involves pure three-dimensional growth that results in clustering of the deposited material into small islands [23]. The Stranski-Krastanow mode initiates layer-by-layer growth of the material and subsequently culminates in three-dimensional island formation.

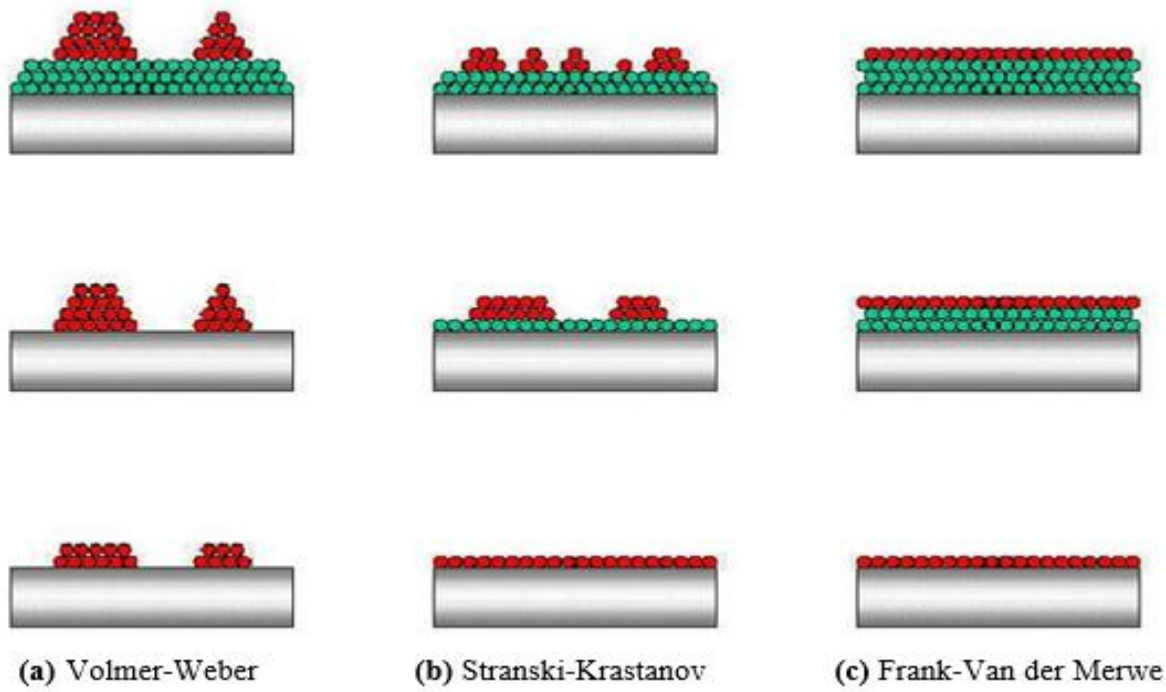

Figure 2.2. An illustration of the fundamental epitaxial growth modes [23].

Basic distinction between the FVM and the V-W modes can be made based on surface and interface tension. In the FVM mode the interaction is weaker between neighboring atoms than with the atoms of the substrate:

$$\nu_B \geq \nu_A + \nu_F$$

Where, ν_A and ν_B are the film-to-substrate and the surface-to-vacuum surface tensions and ν_F is the film-to-substrate surface tensions. Whereas, the case for V-W mode is exactly the opposite.

$$\nu_B < \nu_A + \nu_F$$

Many factors play a role in the S-K growth mode, but the most relevant requirement for the growth of QDs is the presence of a certain lattice mismatch between the substrate and the film.

2.2 Pseudomorphic and metamorphic growth modes

Heteroepitaxy is the epitaxial growth of crystalline material on a crystalline substrate of a different material. If the epitaxial layer's lattice constant is smaller or larger than that of the substrate, it is said to be lattice-mismatched. Usually, the epitaxial layer has a lattice constant more relaxed than that of the substrate [32]. The lattice mismatched is defined mathematically as

$$f = \frac{a_e - a_s}{a_s}$$

where, a_e and a_s are the equilibrium lattice constants of the epitaxial layer and the substrate, respectively. In heteroepitaxial systems with lattice mismatch of $|f| \leq 2\%$, the growth of the initial few epitaxial layers tends to be coherent, or pseudomorphic, in nature. In simple words, the epitaxial layer tries to take on the lattice constant of the substrate in the direction of the growth plane. The general assumption here is that the substrate is thick enough that it is unstrained and is not affected by the epitaxial growth of subsequent layers. Figure 2.3 illustrates the epitaxial growth of two lattice-mismatched materials.

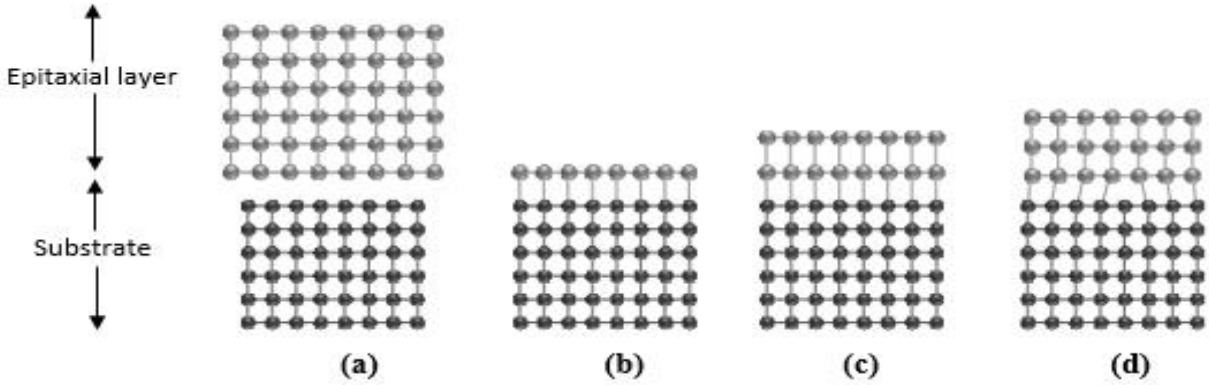

Figure 2.3. Epitaxial growth of lattice-mismatched materials. (a) depicts the equilibrium crystal structures of substrate and epitaxial layer. (b) represents pseudomorphic growth of the epitaxial layer. (c) shows the thickness of the epitaxial layer approaching critical thickness. (d) illustrates the formation of a misfit dislocation (MD) when the layer thickness has exceeded the critical value and has resulted in the epilayer becoming metamorphic [33].

The substrate has a smaller lattice constant than the deposited layers ($a_s < a_e$). Thus, the epitaxial layer has a compressed lattice constant in the direction of the growth plane in order to compensate for the lattice mismatch. This results in an in-plane elastic strain defined as,

$$\varepsilon_p = \frac{a_p - a_e}{a_e}$$

where, a_p is the in-plane elastic constant of the epitaxial layers. With increase in the thickness of the epitaxial layer, there is strain energy built up in the pseudomorphic layer. When this growth reaches a certain layer thickness, called the critical layer thickness, h_c, the strain energy becomes so large that it becomes thermodynamically and energetically favorable for the system to introduce misfit dislocations (MD) at the substrate-layer interface. These MDs in the interface relax some of the strain caused by the lattice-mismatch. In the layers grown beyond the critical thickness, the mismatch is partially accommodated by MDs (plastic strain) and balanced by elastic strain. In this case,

$$\varepsilon_p = f - \delta$$

where, δ is the amount of strain relieved by the introduction of MDs. At this point, the growth is said to be metamorphic in nature and the subsequent partially relaxed layers are referred to as metamorphic layers. Ideally, the value of h_c can be determined from the lattice mismatch and elastic properties of the different materials in the system. However, in practice h_c is tricky to determine accurately, as it is also affected by growth conditions [34].

The typical epitaxial growth mode for moderately mismatched (f in the range of 0 to 2%) InGaAs grown on GaAs substrate begins as a pseudomorphic layer-by-layer growth, followed by formation of MDs at the critical thickness, h_c, and ends in metamorphic layer growth, which is the result of plastic strain relaxation [35]. As the mismatch becomes more prominent, the three-dimensional Stranski-Krastanow growth becomes the most energetically favorable consequence of strain relaxation. The InAs QD samples investigated in this thesis are grown in Stranski-Krastanow mode. The principles of the Stranski-Krastanow growth mode are discussed in detail in the following section.

2.3 Stranski-Krastanow growth of InAs quantum dots

Misfit-driven Stranski-Krastanow (S-K) growth is one of the most commonly used methods to grow self-assembled QDs. Ivan Stranski and Lyubomir Krastanow theoretically proposed this mechanism as early as in 1937 [36]. However, it was only in 1985 that the formation of self-assembled semiconductor QDs based on strained heterostructures was experimentally observed in the InAs/GaAs system [37]. Consequently, experiments carried out in the mid-1990s [38], [39] demonstrated that a 7.2% mismatch in the lattice of InAs/GaAs system facilitates controllable growth of three-dimensional nanoscale QDs by S-K growth mode.

During the S-K growth of InAs QDs, arsenic and indium fluxes are simultaneously supplied to the substrate. The initial stage of growth is in the form of a two-dimensional wetting layer (WL) on a lattice-mismatched substrate, as shown in fig. 2.4 (b), and gives rise to the formation of strained monolayers. This pseudomorphic layer-by-layer growth continues until the film thickness reaches a critical value, h_c, which is inversely proportional to the misfit strain at the epilayer-substrate interface. After a critical thickness of typically 1-2 monolayers (critical thickness for InAs is 1.6 monolayers), nucleation of InAs into three-dimensional islands begins to take place in energetically favorable locations where local strain is accommodated.

Therefore, the structural symmetry of the QDs is fundamentally linked to the strain symmetry of the substrate. Fig 2.4 (c) shows how the nucleation occurs on the strained monolayer.

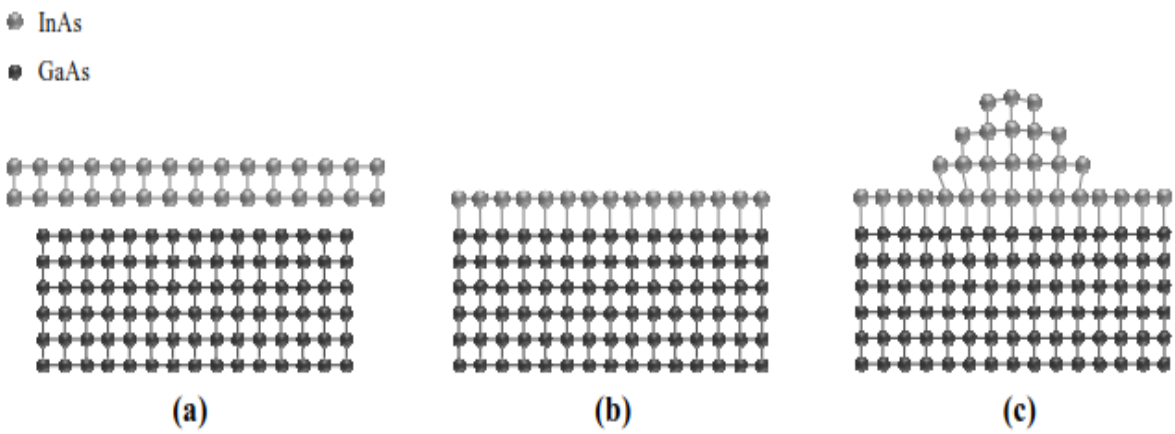

Figure 2.4. Illustration of the Stranski-Krastanow growth mechanism of InAs QDs on GaAs substrate. **(a)** the equilibrium crystal structures of InAs and GaAs are shown. **(b)** depicts the formation of a two-dimensional InAs WL over the substrate. **(c)** When the critical layer thickness, h_c, is exceeded, InAs nucleates into a coherent three-dimensional island [33].

Formation of self-assembled InAs QDs (SAQD) in SK growth mode is a statistical process that is dependent on growth parameters such as InAs growth rate (GR), substrate temperature (T_s), and the ratio of In and As fluxes. These growth parameters control the structural properties of the SAQDs. When the In flux hits the surface, In adatoms migrate on the surface until they reach an energetically favorable location. The average distance that an adatom travels, called the migration length, can be controlled by the growth parameters. The GR and T_s also determine the InAs coverage, θ, which plays a crucial role in the SK growth of SAQDs. The average height and base width of InAs SAQDs are in the range of 2 to 12 nm and 10 to 50 nm respectively, while the dot density ranges from $1x10^8$ to $1x10^{11}$ cm^{-2} [40]. A direct consequence of the statistical nature of formation of SAQDs is that they are randomly distributed on the surface with their sizes varying according to a Gaussian distribution [41].

2.4 Effect of capping on the structural properties of quantum dots

After the InAs SAQDs are grown, an overgrown GaAs capping layer is generally required to provide a well-defined confinement potential. Strong changes can occur to even morphologically well-defined QDs during the capping process. Therefore, it is not prudent to consider the shape of buried QDs to be the same as uncapped QDs. Buried QDs are typically shallower than uncapped QDs. To understand this distinction in energy levels, it is important to study the initial stages of the capping process.

While the GaAs capping layer is forming, the GaAs tends to avoid the apexes of the InAs QDs because they are energetically unfavorable. Thus, in the initial stages of capping, there is no GaAs growth on top of the elastically relaxed InAs islands. While the InAs QDs are covered by the GaAs capping layer, they experience a dramatic reduction in their heights [41], [42]. This reduction of QD height is controllable through GaAs growth rate and temperature. Because of the GaAs overgrowth, the elastic energy in the InAs QDs increases significantly due to a decrease in the elastic strain relaxation. The surface energy of InAs is lower than that of GaAs surfaces, which results in In atoms detaching from the top of the QDs and migrating to the newly-formed GaAs surfaces, and thus creating a second WL [43], [44]. This process is illustrated in figure 2.5. Eventually, the QD height stabilizes due to the influx of stray In atoms and Ga atoms that cover the sides of the QDs.

Finally, as the GaAs capping proceeds, the QDs end up covered by GaAs. The rise in elastic energy during the overgrowth process, in addition to abrupt composition gradient in the QD-GaAs interface results in a mixture of In atoms from the QDs and Ga atoms from the GaAs surfaces. This intermixing process reduces the In content in the InAs QDs significantly and creates various composition gradients based on the overgrowth conditions and original morphology of the QDs [45]–[47]. Therefore, numerous morphologies of QDs can be designed by controlling the InAs QD growth conditions and GaAs overgrowth.

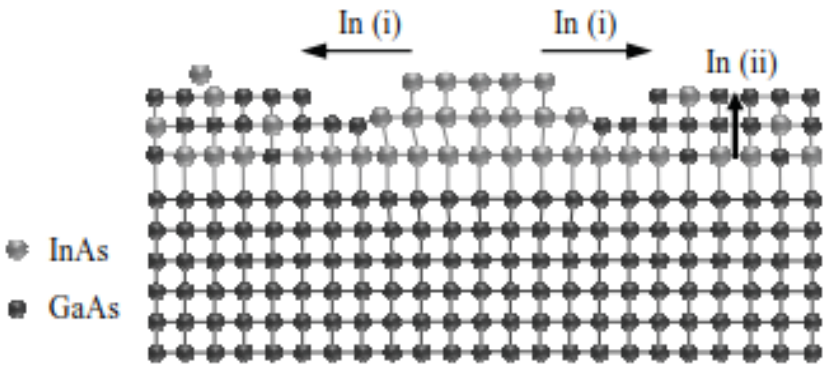

Figure 2.5. Reduction in height of InAs QDs due to migration of In atoms from top of the QDs to the GaAs surface (i) and In atoms from the WL shift to surface (ii) [33].

Depending on the conditions used for capping the QDs, a less or more pronounced smearing of the QD structure can be achieved. This is important because changes in the physical structure and the chemical composition have a noticeable effect on the energy bandgap of the InAs/GaAs system, thus allowing the QD emission properties to be highly tunable. For instance, a lower concentration of In in the QDs affects the energy bandgap of the QDs, resulting in changes in the resonant energies required for excitation.

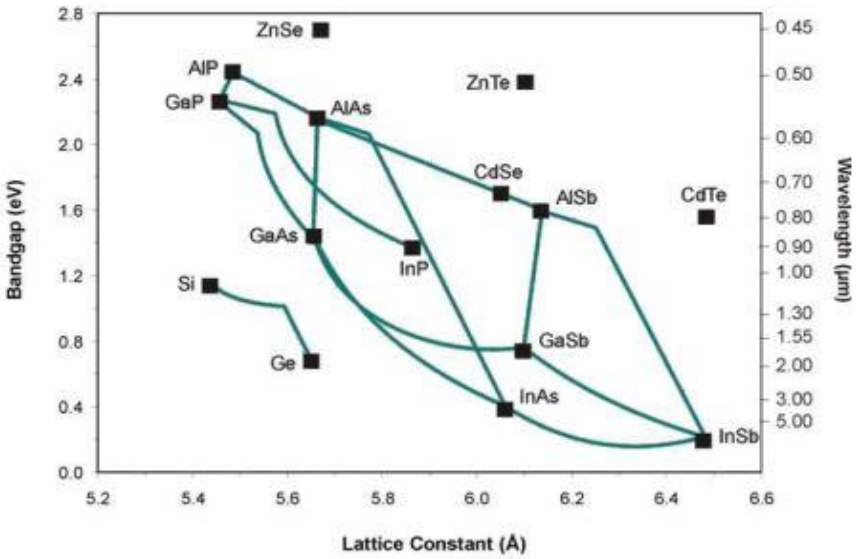

Figure 2.6. Relationship between bandgap and lattice constant for various III-V compunds [48].

2.5 Confined states and optical properties

The electronic structure of quantum dots defines their optical properties. An important parameter that determines the optical properties of semiconductors is the density of states (DOS) for charge carriers, which describes the number of quantum states per unit energy. The DOS is strongly affected when the physical dimensions of a structure become small enough to confine electrons and holes in more than one dimension.

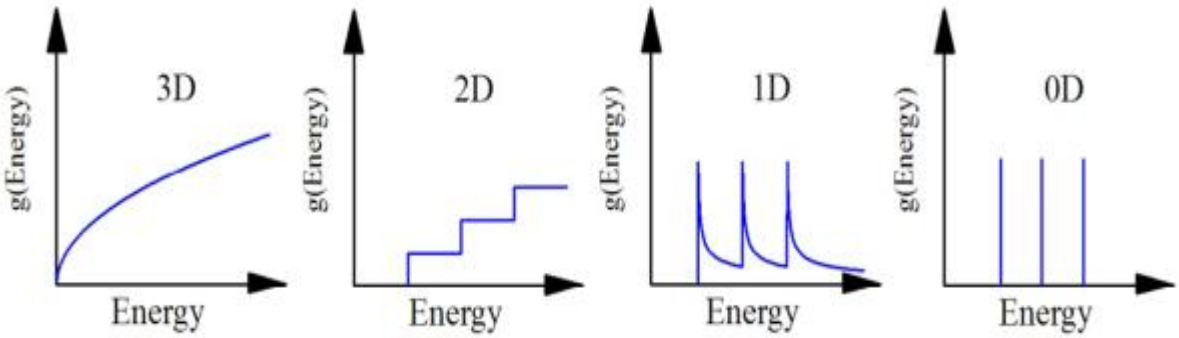

Figure 2.7. Graphical representations of DOS for 3D, 2D, 1D and OD structures [49].

In the 1970s, quantum confinement of charge carriers in one dimension resulted in quantum wells (QW) and their successful application in laser technology [50]. The threshold current of QW lasers were reduced by one order of magnitude compared to their bulk heterostructure laser counterparts. This opened up a relatively new path to design ultra-efficient devices with one or more dimensions of confinement (examples: quantum wire, quantum dot). The number of available energy states near the band edge results in higher confinement of the structure. According to Fermi's golden rule, the overlapping of electron and hole wave functions due to spatial localization leads to an increase in the probability of optical transition. Fermi's golden rule states that the rate of spontaneous emission depends directly on the number of available energy states.

$$W_{if} = \frac{4\pi^2}{h}\left|M_{if}\right|^2 g(Energy)$$

where, W_{if} is the transition rate between initial and final states, M_{if} is the optical matrix element and *g(Energy)* is the final density of states. Increase in spatial localization of the carriers due to confinement leads to an increase in M_{if} and *g(Energy)* [51].

In QDs, the charge carriers are confined in all three spatial dimensions, resulting in an atom-like energy structure as shown in figure 2.7. In the case of InAs/GaAs QD system, the bandgap of InAs is smaller than that of GaAs. This allows for efficient trapping of the charge carriers in the InAs QDs. The size of the potential well created by the QD affects the number of available energy states for charge carriers within the QD. The carriers are typically injected optically or electrically into the QDs through the GaAs matrix layer via the InAs WL. If the excitation is substantial, multiple electrons and holes can be trapped simultaneously inside the QD.

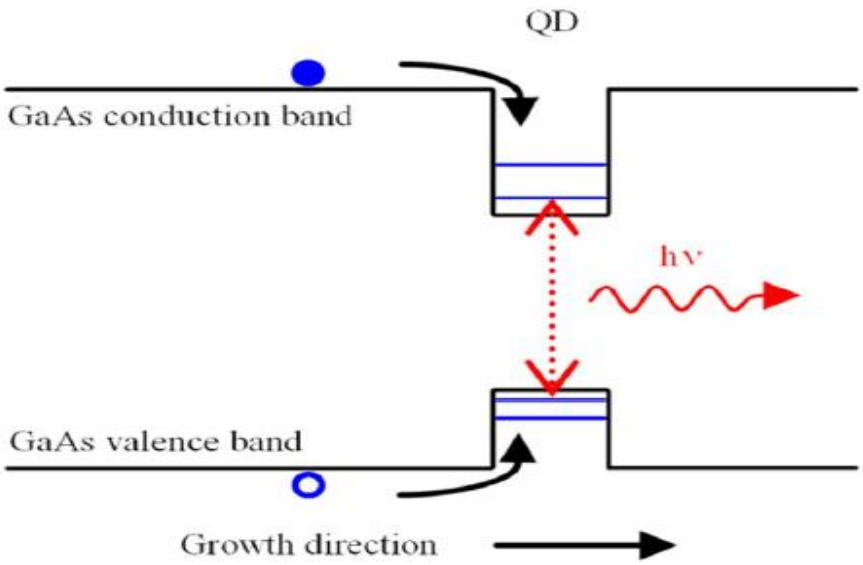

Figure 2.8. Schematic illustration of the energy structure of InAs/GaAs QD system.

At low temperatures, the de Broglie wavelength λ_{DB} is in the range of 10 – 100 nm. At such small dimensions, the thermal energy is smaller than the spacing between energy levels in the structure. Consequentially, the binding energy between electrons and holes due to Coulomb attraction is larger than the thermal energy $k_B T$ leading to the formation of excitons, which decay radiatively with spectra consisting of sharp peaks. The PL emission spectrum of an individual QD shows several extremely narrow peaks that correspond to excitonic states such as neutral single exciton (X), charged single exciton (X*), biexciton (XX) and charged

biexciton (XX*). The schematic representations of excitons are shown in figure 2.9. A neutral single exciton contains an electron-hole pair, while a charged single exciton has an additional electron or hole. Similarly, a biexction contains two electron-hole pairs confined in the QD, while a charged biexciton contains an additional electron or hole.

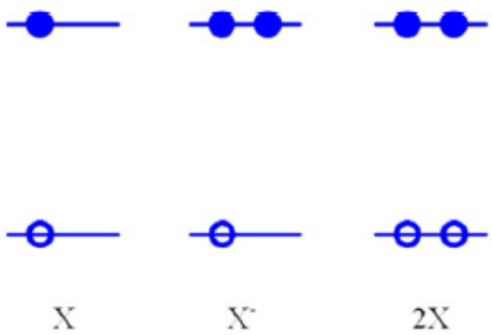

Figure 2.9. An illustration of the different types of excitons that can be formed [49].

An exciton's spatial extent in a dielectric medium is determined by its Bohr radius, a.

$$a = \frac{4\pi\varepsilon_0\varepsilon_r\hbar^2}{\mu^* e^2}$$

where, ε_r is the relative permitivitty of the medium and μ^* is the reduced electron-hole effective mass. Typically, it is more convenient to describe a QD as an entity that occupies a region of space with sizes comparable to the Bohr radius rather than considering λ_{DB} for electrons and holes separately. With respect to atoms, QDs proffer the advantage that they can be embedded into a solid state matrix because of their fixed position in space.

A QD can be optically excited in various ways, depending on where the photo-excited carriers created. One method is to create a reservoir of charge carriers in the surrounding material by tuning the laser to excite electrons into the conduction band of the WL or the GaAs matrix. The charge carriers then relax to lower energies, through scattering, and fill up the quantized energy levels of the QD and spontaneously recombine to emit a photon. Another method, called quasi-resonant excitation, consists of tuning the laser energy to the higher energy states within the QD. In resonant excitation, a laser is finely tuned to the bandgap of the QD. For an InAs/GaAs QD system in this thesis, the resonant excitation wavelength is 850 nm, while the quasi-

resonant excitation wavelength is 895 nm. The non-resonant excitation wavelength used in experiments is 640 nm. As evident from figure 2.10, each optical excitation scheme individually excites different parts of the energy band.

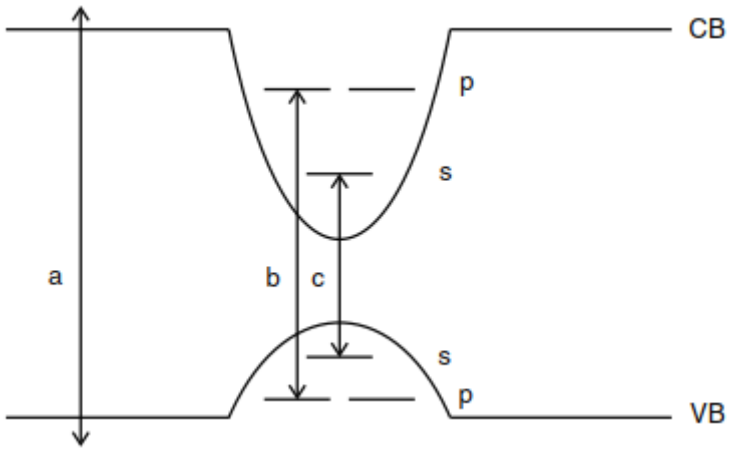

Figure 2.10. (a) non-resonant, **(b)** quasi-resonant, **(c)** resonant optical excitations [52].

To incorporate QDs into optoelectronic devices, they are capped by a semiconductor layer. This efficiently reduces unwanted nonradiative recombination on surface states. Optical properties of QDs are strongly affected by the capping layer. Radiative recombination of an exciton in a QD results in emission of a characteristic photon. The energy of the emitted photon is equal to the energy difference between the electron and hole states. Primary parameters that affect a QDs energy states are the chemical composition and height of the QD. For InAs/GaAs QDs, the emission energy is reported to fall in the range of 1.4 eV, for shallow QDs, to 0.8 eV for deep QDs [53] (as described in Figure 2.11). In this thesis, the emission wavelength range of the QDs is tuned to fall in the range of 930 nm to 950 nm.

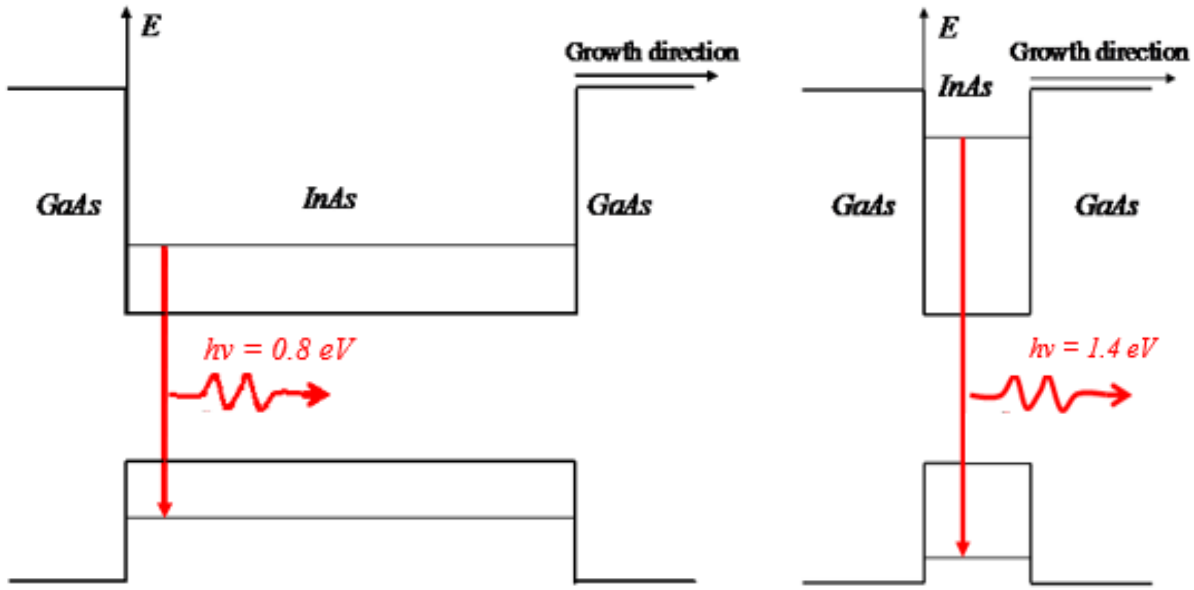

Figure 2.11. A schematic representation of a deep QD (left) and a shallow QD (right) and their corresponding emissions.

Stray electrical charges from adjacently situated QDs cause the emission energies of, for example, excitons and biexcitons to differ. Therefore, while studying the optical properties of single QDs, resonant excitation excitation along with a very narrow area of PL collection is necessary for high quantum efficiencies and long coherence times of the emitted photons. Single-photon emission from QDs is based on the cascaded emission process, where the last photon emitted after a very short excitation pulse is separated in energy from the others. This facilitates for the isolation of photons, thus making the QD a potential single-photon source [12].

Chapter 3

3 Research Methodology

3.1 Sample growth by molecular beam epitaxy

The samples studied in this thesis were grown in a VG V80 MBE reactor, which consists of a sample preparation chamber and a growth chamber. This system is equipped with indium, aluminium and gallium effusion cells as group III sources and phosphorous and arsenic crackers as group V sources. The various steps in the growth process are mentioned below.

1. Annealing of GaAs substrate in the sample preparation chamber for 60 minutes at 250° C. It is done to remove any contaminants or water molecules that might be present on the sample or sample holder.
2. Annealing of the sample in the growth chamber for 10 minutes at 615° C. This is an important step performed to remove oxides from the substrate.
3. Growing 100 nm GaAs buffer layer on top of the GaAs substrate at 580° C with a growth rate of 0.3 µm/h. The buffer layer is grown to minimize the surface roughness of the GaAs substrate and to improve surface quality.
4. Growing 100 nm Al (0.7) Ga (0.3) As buffer layer at 580° C with a growth rate of 1µm/h. The AlGaAs buffer layer acts as a charge-confinement layer. It prevents any stray charges in the upper layers from entering the substrate.
5. Growing 100 nm GaAs layer at 580° C with a growth rate of 0.3 µm/h. The InAs QDs are embedded in this GaAs layer.
6. Growing InAs QDs at 533° C with a growth rate of 0.05 µm/h. The V/III beam equivalent pressure (BEP) denotes the ratio of the group V flux to the group III flux. In this case the BEP (As/In) = 30.
7. Capping the InAs QDs with GaAs overgrowth layer at 533° C.
8. Rapid cooldown of the sample under As flux.

While growing the QD layer, a very precise amount of material was used to grow the WL. A very slow growth rate is necessary to control the amount of material exposure accurately. These parameters strongly determine the morphology of the QDs that are formed. Another important

growth parameter is the growth temperature, which affects the density of QDs in the sample. It is a simple case of the Goldilocks principle. If the temperature is too high, too much material from the epilayer is evaporated, resulting in a lack of QD formation. If the temperature is too low, the density of the QDs is very high, resulting in agglomerations or clumping of QDs. Therefore, it is important to find the right growth temperature for a particular material system. During the growth of samples used in this thesis, there was a temperate gradient of 5 to 10 ^{o}C present over the sample. This variation in temperature across the sample resulted in a gradual decrease in the density of QDs towards the sample edge.

The next few lines provide a brief description of the basic physical structure of QDs fabricated in this thesis. A circular GaAs (100) wafer of 350 µm thickness was used as the substrate. A 100 nm GaAs buffer layer was grown on top of the substrate. Then, 100 nm of Al (0.7) Ga (0.3) As was grown, which acts as a charge-confinement layer. Next, a 100 nm GaAs layer, called the GaAs matrix, was grown. A very thin InAs WL was grown on top of the GaAs matrix. Once the thickness of the WL exceeded the critical value, InAs QDs began to form on the GaAs matrix layer. An overgrowth of GaAs capping layer was done after the embedded QDs were formed.

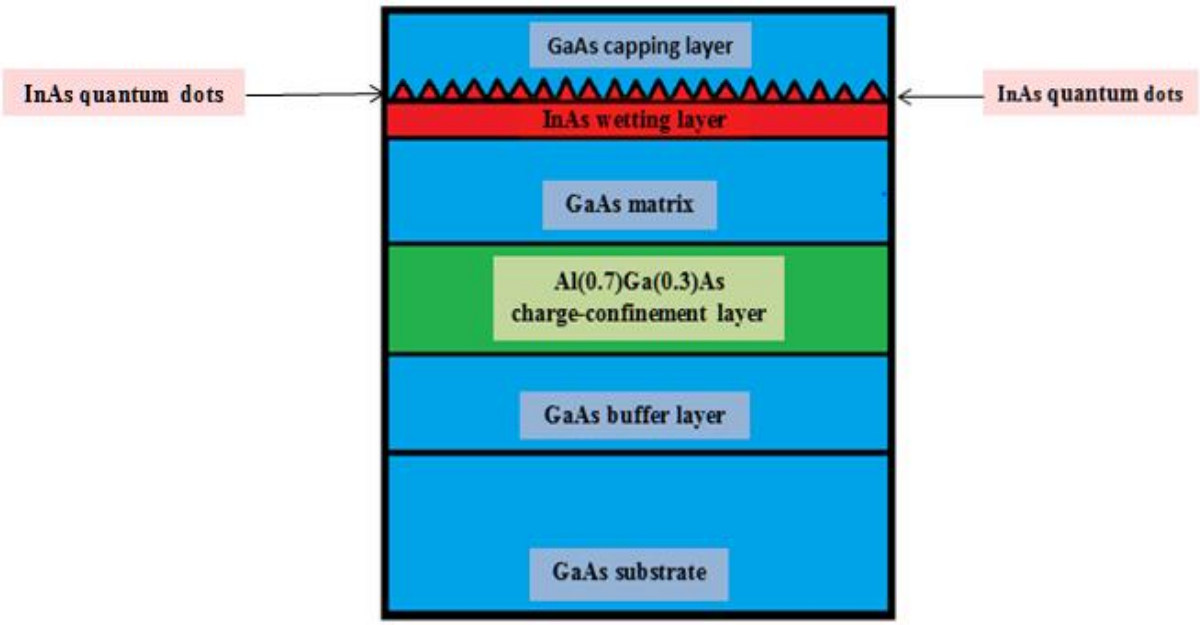

Figure 3.1. Basic schematic of the samples grown without surface dots.

Two types of samples were grown based on different overgrowth processes. For the experiments performed to investigate optical properties of QDs in this thesis, samples with varying GaAs capping layer thicknesses were fabricated. The various capping layer thicknesses

are 20 nm, 30 nm, 40 nm and 60 nm. This means that the InAs QDs are situated at 20 nm, 30 nm, 40 nm and 60 nm distances from the top of the capping layer (i.e. sample surface. Figure 3.1 shows the basic schematic of the samples with GaAs capping layer. This set of samples (with varying GaAs capping layer thickness) was used for studying the effects of QDs that are close to the sample surface (at varying distances of 20 nm, 30 nm, 40 nm and 60 nm).

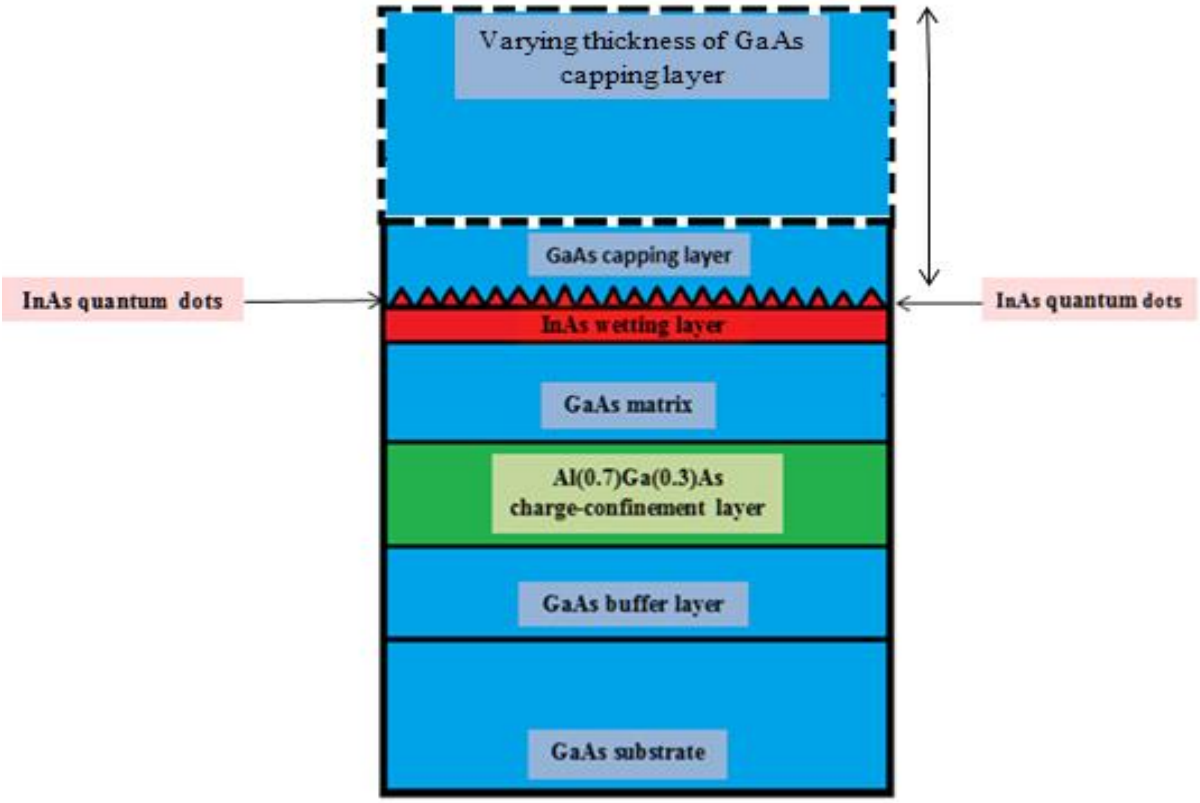

Figure 3.2. A schematic of the samples that have undergone overgrowth of GaAs capping layer. The GaAs capping layer thickness has 4 different thicknesses: 20 nm, 30 nm, 40 nm and 60 nm.

A second set of samples was grown with the same basic structure. But, in addition to the InAs QDs that are embedded in the GaAs matrix, a layer of QDs was grown on top of a 100 nm GaAs capping layer (as shown in figure 3.3). These surface QDs provided the opportunity to study the structural properties. It must be noted that even though the surface dots were subject to rapid cooling immediately after they were grown, some diffusion of some In atoms took place across the surface (refer figure 2.5). This means that the surface dots have significantly different morphologies (in terms of QD height, width and composition) compared to the QDs embedded in the GaAs matrix. Therefore, the surface QDs provide reliable information about

the QD density in the sample. However, they do not necessarily exhibit the same morphologies as the embedded QDs.

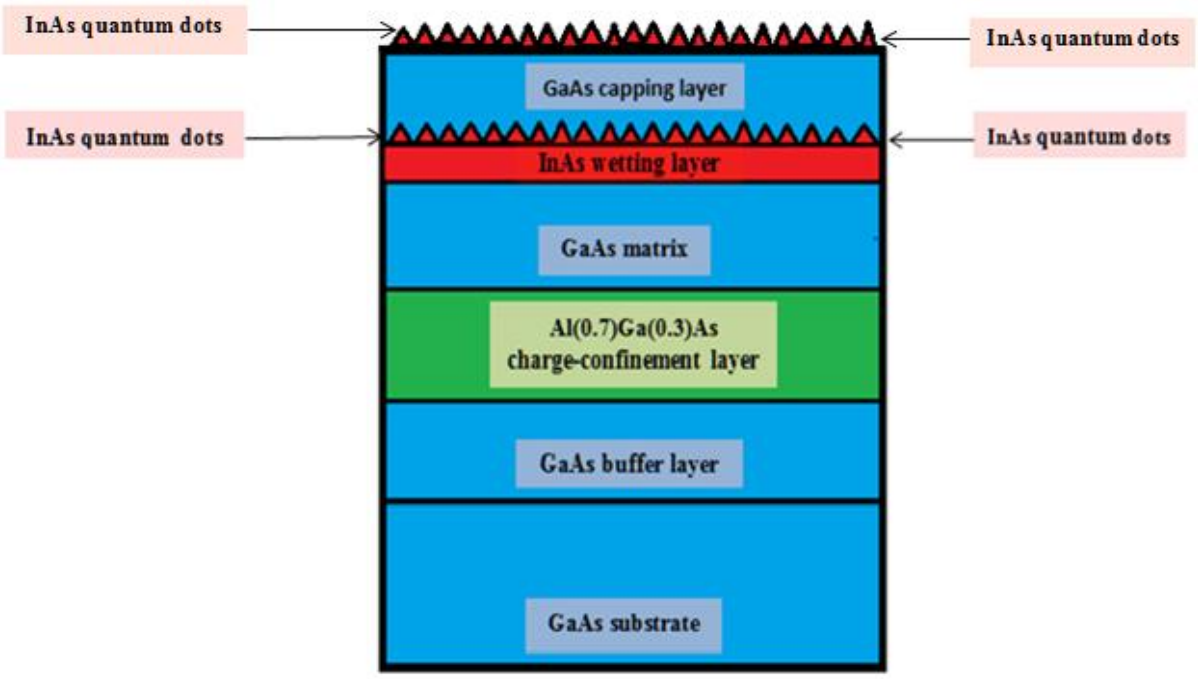

Figure 3.3. Basic schematic of the samples grown with surface dots on top of a 100 nm GaAs capping layer.

Only the embedded QDs are optically active. Nonradiative surface recombinations are dominant in QDs on the surface. However, since the QDs at the surface were fabricated under identical growth conditions as the embedded ones, the density of the active QDs can easily be determined by scanning electron microscopy (SEM) of the sample surface.

3.2 Scanning electron microscopy

Scanning Electron Microscopy (SEM) is a useful method to study a sample's surface in detail. A narrow electron beam studies the surface that is sometimes coated with a thin film of gold or platinum to maximize contrast and signal-to-noise ratio [54]. At present, SEM greatly helps in understanding the surface characteristics of nanostructures, mainly due to significant progress in SEM for imaging and elemental analysis in terms of resolution (both spatial and lateral) and sensitivities [55], [56]. The basic components of SEM are the electron gun, electric or magnetic lenses, deflection coils and detectors. The electron gun is usually consists a heated Tungsten filament that generates a high-energy electron beam.

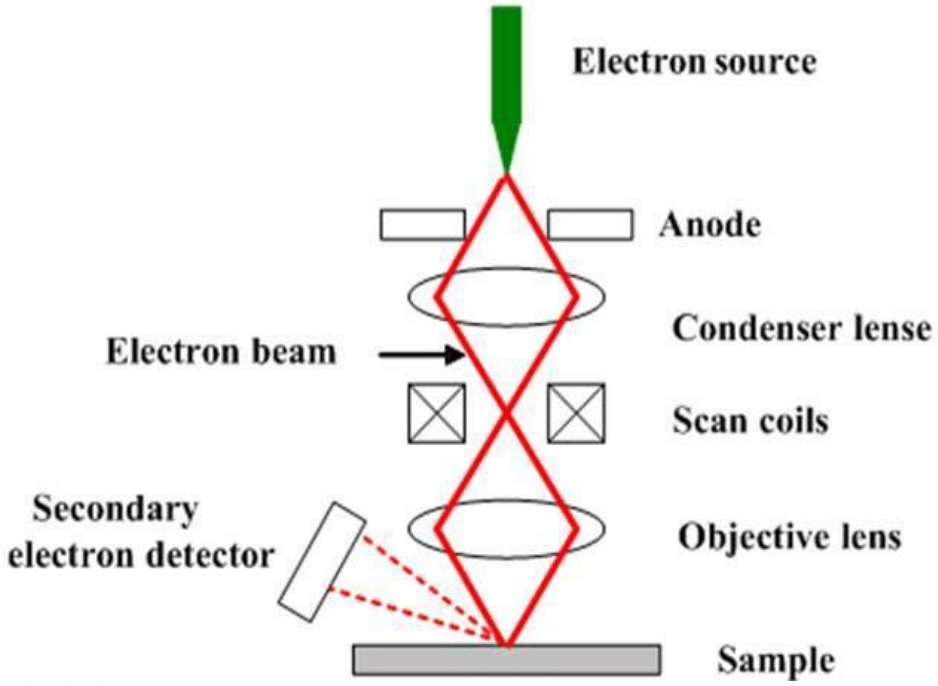

Figure 3.4. A basic schematic diagram of scanning electron microscopy.

The beam is accelerated and collimated into a probe using electric or magnetic fields, after which it is focused through the condenser lenses onto the sample surface. The entire chamber is maintained under total vacuum in order to maintain the collimation of the electron beam. Without a vacuum, the electron beam would experience interference from air particles that would distort the images obtained from the surface. The deflection or scan coils help in

controlling the movement of the beam spot over the surface of the sample and the beam is then projected towards the sample by the objective lenses. Fig 3.4 shows the basic schematic of SEM with its components.

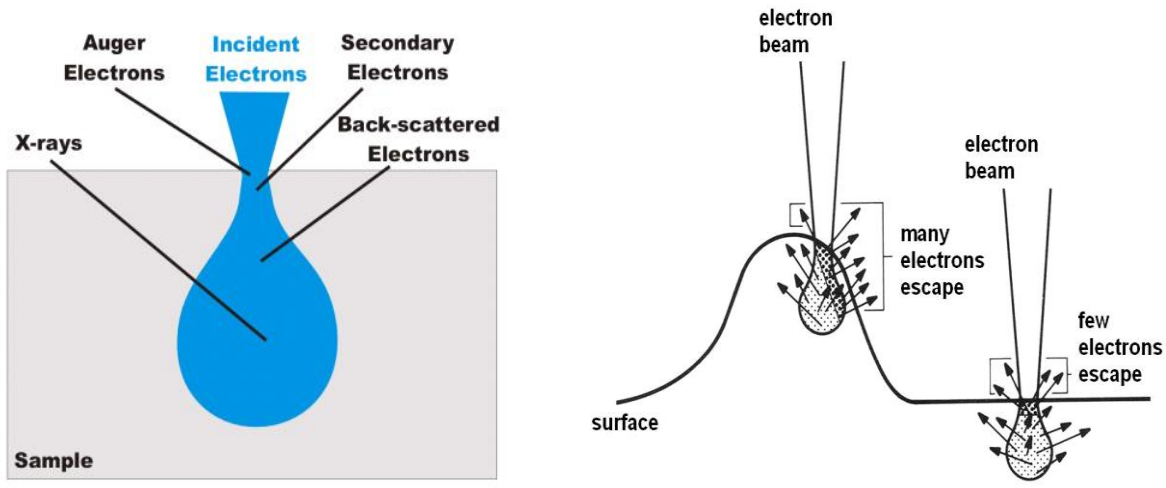

(a) **(b)**

Figure 3.5. (a) Gives an illustration of the interaction volume in an SEM. It shows various emissions that occur when an electron beam strikes the sample surface. **(b)** Demonstrates the "edge effect", according to which there is an increased emission of electrons from edges and peaks.

The electron beam-turned probe raster-scans across the sample surface. The scanning results in interactions between the sample surface and the electron beam resulting in various types of emissions that are captured by appropriate detectors. The most important of these interactions are the ones that produce backscattered electrons (energies larger than 50 eV) and secondary electrons (energies lesser than 50 eV) which provide morphology/surface topology and elemental composition information respectively, while a more detailed compositional information can be obtained by detecting characteristics X-rays from the interactions [57]. There are separate detectors for backscattered and secondary electrons. Fig. 3.5 (a) shows the interaction volume between the electron beam and the sample surface. Different interactions take place at various depths of the sample, leading to impacted electrons that are distinguishable

in energy. The backscattered electrons are the product of an elastic scattering between the electron beam and the sample. The atomic number of the atoms in the sample determines the probability of occurrence of elastic scattering. Hence, backscattered electrons provide great compositional information. The secondary electrons that are generated from inelastic scattering have sharp contrast on surface topography of the sample. This sharp contrast from secondary electrons is governed by the edge effect: the number of secondary electrons emitted from edges and peaks is more than the number from flat areas and depressions, therefore leading to increased brightness from sharp features. The edge effect can be reduced by lowering the energy of the incident electron beam. This also results in lower backscattered electrons emission, improving the contrast in secondary electron images. The edge effect is depicted in fig 3.5 (b).

In this thesis, signals from secondary electrons were used to characterize the InAs/GaAs quantum dot samples based on the quantum dot densities and QD size. The SEM setup used for obtaining images for this thesis was the Carl Zeiss Ultra-55, which has an in-lens detector to detect secondary electron signals. The images from the SEM were analyzed using ImageJ software and WSxM 5.0 develop 9.0 software. The area of study in every SEM image was identified using ImageJ software, which was used to translate the number of pixels into the area of study. WSxM is designed to analyze scanning probe microscopy images but it can also provide qualitative information about the topography of samples from gray scale images in TIFF format [58].

3.3 Atomic force microscopy

An atomic force microscope (AFM) is a scanning probe microscopy technique that helps in obtaining high-resolution, 3-dimensional topographic and surface morphology images of a sample. It has a lateral resolution in the order of 1 nm and a vertical resolution of less than 0.1 nm. As with the other scanning probe techniques, in the AFM too, a probe scans over the sample and the forces present between the probe's tip and the sample's surface are measured. The forces of interaction (either attractive or repulsive) between the tip and the sample fall under a wide range of categories such as Van der Waals, electric, thermal, magnetic, etc. Each technique might have different hardware components and software for processing but the

underlying principle is the same. One major advantage the AFM holds over its predecessor, the scanning tunneling microscope (STM), is its ability to study insulators, in addition to metals and semiconductors. This is not possible when using an STM since its operating principle depends on a measuring an electrical current (tunneling current) between the tip and the sample's surface. Whereas, the AFM opens up the possibility to study the physical forces of interaction between the tip and an insulator's surface that results in high-resolution topographic images.

The principle of AFM is to measure a force of interaction between a probe's very sharp tip (in the order of 10 nm) and the sample's surface. Figure 3.6 represents the operating principle of AFM. The tip is at the end of a small, flexible cantilever.

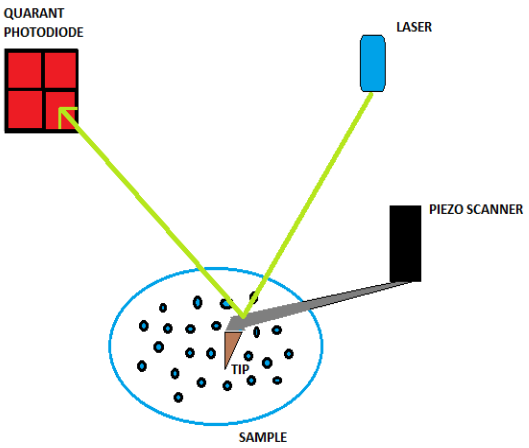

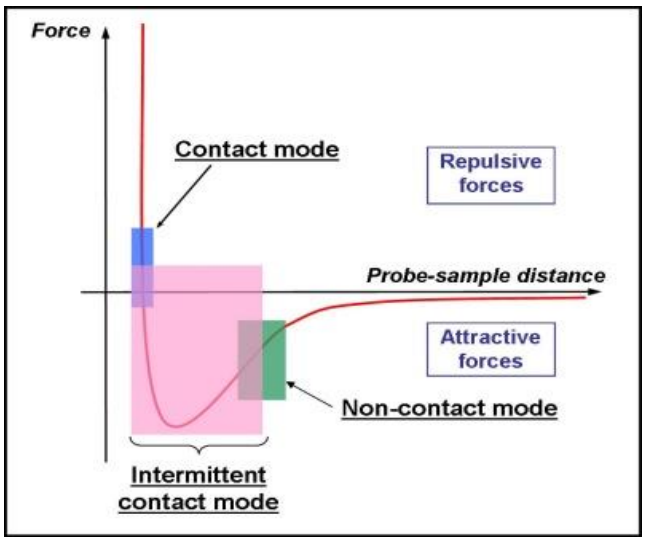

Figure 3.6. Operating principle of AFM with all its components. **Figure 3.7.** A graph displaying the various modes of operation in AFM.

The cantilever is mounted on a piezoelectric scanner that moves in the horizontal as well as the vertical direction when voltage is applied appropriately to the X, Y and Z electrodes. There are three modes of operation of an AFM: Contact mode, non-contact mode and tapping mode. Figure 3.7 gives an illustration of the relationship between the interaction force and the tip-to-sample distance in the three different modes of operation. Each mode has its own merits and demerits depending on the sample and the conditions. In this thesis, the AFM was operated in the intermittent contact mode, in other words, tapping mode. In this mode, the cantilever ideally

operates at its resonant frequency. As the tip moves towards the sample surface, it experiences a deflecting force. This opposing force in turn affects the resonance of the cantilever. A laser beam from a diode laser bounces off the top of the cantilever and hits a quadrant photodiode. The change in the cantilever's operating frequency is determined by translating the changes in the position of the laser beam spot on the photodiode to change in frequency. For the experiments, Digital Instruments (Veeco) Dimension 3100 AFM was used to analyze the topography of various samples. The most important application of the AFM in this thesis was to determine the heights of QDs in different regions of the sample. WxSM software was used to analyze the topographic images from the AFM. It is a freeware application that is dedicated for analyzing and processing scanning probe microscopy data.

The samples that were studied using the AFM had QDs on top of the GaAs capping layer (shown in figure 3.3). The experiments were carried out in such a way that in each sample, QDs that were at varying distances from the center of the sample were studied. For example, in sample K7451, the QDs at distances of 0 mm, 2.5 mm, 5mm and 7.5mm from the center of the sample were studied. This procedure was followed in order to study the profiles of the QDs in different areas of the sample, thus collecting information about changes in QD morphology with respect to growth temperature. More information on the results of these experiments using the AFM is presented in section 4.2.

3.4 Photoluminescence microscopy

Photoluminescence spectroscopy measures the spontaneous emission of photons that are generated by the recombination of confined charge carriers. The electron-hole pairs (excitons) are created from optical pumping of a semiconductor by an excitation laser. When a semiconductor is optically excited, electrons jump from the valence band to the conduction band (provided the optical pumping energy equals the bandgap of the material), while holes occupy vacant states in the valence band. These excited electron-hole pairs may either undergo radiative recombination by emitting a photon of energy equal to the bandgap of the semiconductor material or nonradiative recombination via thermal relaxation (resulting in phonons [59]). Non-radiative recombination takes place at impurity sites and defect centers in the material and they end up as excess states in the bandgap. Nonradiative recombination

occurs at material surfaces where dangling bonds on material surfaces form surface states. Surface recombination is an unwanted phenomenon while investigating QDs. The effect of surface states can be minimized by passivating with a material of larger bandgap that prevents carrier diffusion to the surface states [60].

In this thesis, two different PL setups were used to conduct preliminary studies of the QD samples. Room temperature PL measurements were performed using an Accent RPM2000 PL mapper. A laser beam illuminates the sample and the PL is detected with a charge-coupled device (CCD). Low-temperature PL spectroscopy (LTPL) was used to study the PL spectra from an ensemble of QDs in a particular area of the sample. As mentioned in section 4.1, there is a variation in QD density across the sample due to a temperature gradient present during their fabrication. Using LTPL spectroscopy, PL responses from different areas of the sample are studied. Some important results are obtained from the PL responses. The position of the PL peak on an energy scale denotes the average ground state energy of a QD ensemble. This information is useful when selecting areas of the sample with respect to the QD emission wavelength. Another essential detail from PL spectra is the width of the PL peak. The wider the peak is, the more uniformly distributed the QDs are (with respect to emission wavelength). This is important feedback for fabricating subsequent QD samples. For LTPL experiments, the excitaiton source was a variable-power laser beam of 532 nm wavelength . The measurements were conducted at temperatures ranging from 13.5 K to 15.4 K. The laser light passed through a chopper that rotates with a frequency of 225 Hz. The results obtained from LTPL experiments are presented in section 4.3.

3.5 Micro-photoluminescence spectroscopy and imaging

Micro-photoluminescence (μ-PL) spectroscopy is a robust and a versatile tool for investigating the optical and electronic properties of individual nanostructures. A laser excites charge carriers from occupied states to empty states. The photo-excited charge carriers recombine after an extremely short period and emit a characteristic photon (spontaneous radiative recombination), giving rise to a PL signal. In conventional PL spectroscopy, ordinary macroscopic lenses collimate and direct the laser beam on the sample. The spatial resolution of conventional PL

spectroscopy might be good enough to characterize bulk materials and ensembles but it becomes insufficient to investigate individual nanostructures. Though the principle of operation of µ-PL spectroscopy is the same as a regular PL spectroscopy, microscopic objectives in µ-PL setups allow a better spatial resolution.

In this thesis, the investigation of optical properties of individual QDs was carried out with the µ-PL setup schematically shown in Figure 3.8. The samples were mounted on an XYZ-piezo stage inside a low-vibration closed-cycle helium cryostat (which can be cooled down to 5K) enclosed by a vacuum shroud. The vacuum shroud effectively maintains UVH conditions inside the sample chamber, thus protecting the sample from being exposed to atmospheric contaminants. A piezo controller controlled the position of the sample along the lateral and vertical directions. For coarse sample alignment, an external light source (in this case, an LED) and a high-resolution camera were used. Laser beams of various wavelengths (640 nm, 850 nm and 895 nm) were used to excite the QDs in order to analyze their PL responses. As the QDs are sensitive to the energy of excitation, the power incident on the sample was monitored

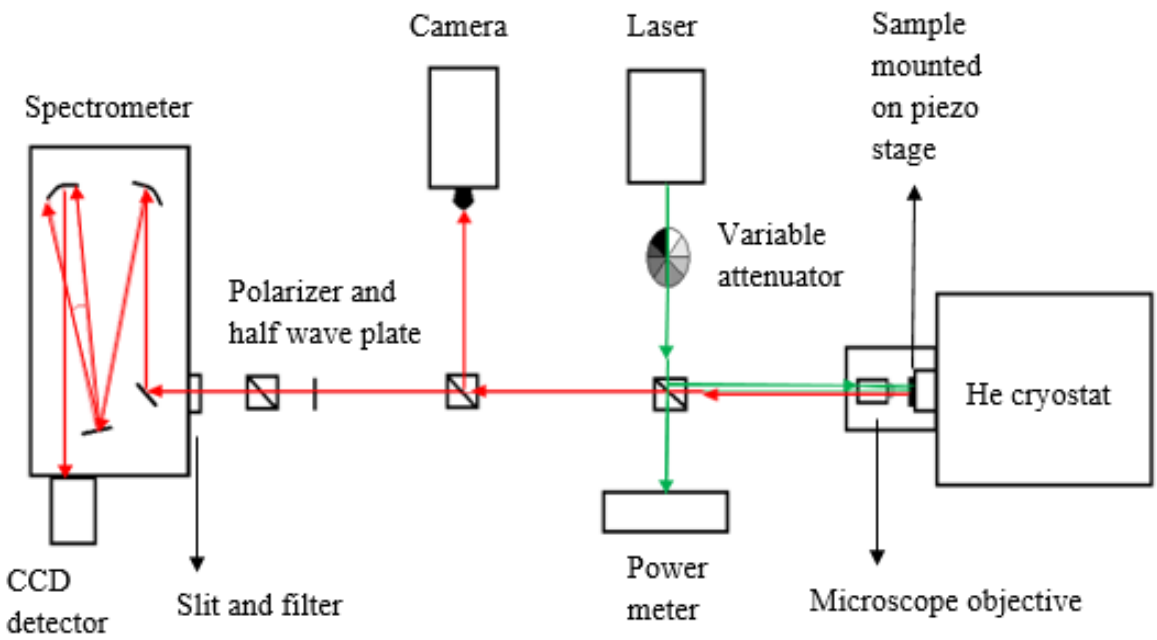

Figure 3.8. A schematic diagram of the µ-PL setup used for investigating optical properties of individual QDs.

by a power meter. The incident power could be varied up to six orders of magnitude using a variable attenuator. The laser beam was focused down to a spot size of 1 µm on the sample with a 50x high numerical aperture objective. This allowed focusing of the beam spot on a single InAs QD on the sample. The resulting PL emission was collected by the same microscope objective and forwarded through an appropriate high-pass filter into a very narrow slit. The slit width was adjusted precisely in order to isolate the PL signal from a very small area on the sample, thus essentially collecting emission from individual QDs. A spectrometer that is equipped with two gratings of 1200 lines/mm and 1800 lines/mm each helped in forming spectral images from the PL response. The spectrometer setup has a spectral resolution of 30 µeV. A Peltier-cooled 2D CCD detector collected the PL response. The axis of the slit, through which the PL emission enters, acts as the Y-axis for the spectral images. After the PL emission from the samples enters the spectrometer, it is dispersed into a spectrum by the grating. This spectrum falls on the 2D detector and forms the X-axis of the spectral images. In addition to conventional PL spectroscopy, polarization-dependent measurements were carried out using a polarizer and a half-wave plate. Time-resolved PL measurements are also possible using the same setup with the help of an additional avalanche photo detector (APD). It is explained in detail in section 3.6. The results from µ-PL experiments are presented in section 4.4.

3.6 Time-resolved photoluminescence spectroscopy

In semiconductors devices, charge carrier dynamics are determined by the architecture and functions of the respective material and directly reflect on the quality and nature of wafer materials. This makes efficient and precise measurement of the charge carrier lifetime an essential requirement for characterizing these systems. For certain classes of semiconductors, the characteristic charge carrier lifetime depends strongly on the nature and dimensions of the materials involved. Furthermore, surface effects and passivation, as well as the influence of possible impurities, dopants and defect sites can play a significant role in variations of carrier lifetime. Since photoluminescence of semiconductors offers a direct insight into the charge carrier dynamics, the general methodology of time-resolved photoluminescence via time-correlated single photon counting is highly suitable for the analysis of the phenomena that determine fast charge carrier dynamics in a semiconductor. In time-correlated single photon counting (TCSPC), the detection of single photons from a periodic/pulsed light signal is performed by measuring the detection times and reconstructing the waveform from the

individual time measurements. TCSPC is based on the fact that for low-level, high repetition rate signals, the light intensity is generally low enough that the probability to detect more than one photon in one signal period is negligible. When a photon is detected, the instant of arrival of the corresponding detector pulse during the signal period is measured. Over the course of several signal periods, a large number of photons has been detected and the distribution of photons over the time period of the signal builds up. The results represent the waveform of the "optical" pulse.

As mentioned in section 3.5, time-resolved photoluminescence spectroscopy measurements can be carried out in the same setup used for μ-PL spectroscopy. The sample is kept in a cryostat and is illuminated by a pulsed laser. The spontaneously emitted light is collected and can be directed either to a charge-coupled device camera for sample alignment or to a spectrometer equipped with a fast single-photon counting avalanche photodiode (APD) for time-resolved measurements. Excitation sources were 640 nm and 850 nm lasers of 80 MHz pulse repetition rate that excite the GaAs matrix and the InAs wetting layer, respectively.

Chapter 4

4 Results and discussions

4.1 Results from SEM

Table 4.1. A compilation of data that shows displaying a changes in QD density with respect to distance.

Distance from the centre of the sample (mm)	Image area (cm^2)	QD density (cm^{-2})
0	17.54	3.27×10^9
2.5	16.86	3.30×10^9
5	17.74	2.82×10^9
7.5	17.77	1.25×10^9
10	17.79	3.57×10^8
12.5	17.69	1.69×10^7

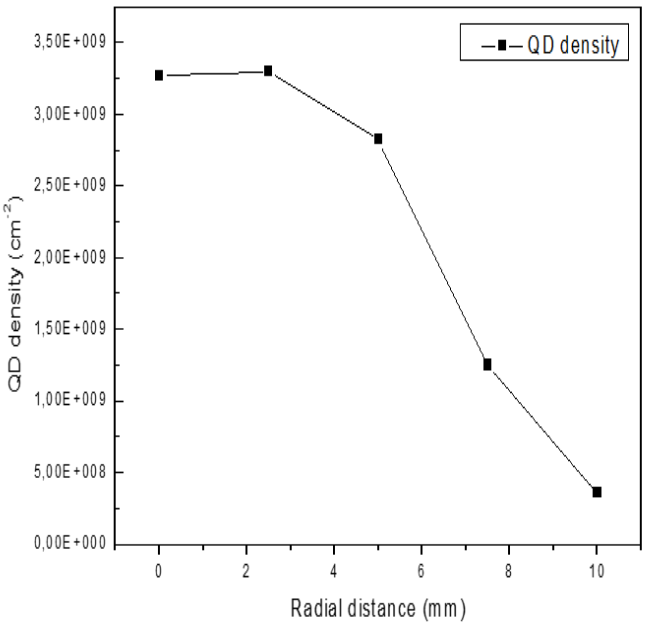

Figure 4.1. A graph of non-linear decrease in QD density from the sample centre across the sample.

The results from SEM analysis are useful to learn about density of QDs on the surface. Consequently, this information is useful to determine the density of embedded QDs. For SEM experiments, samples containing surface dots are considered. From table 4.1, it is evident that there is a non-linear decrease in QD density as we move away from the centre of the sample. Figure 4.1 depicts a graph that compares QD density with radial distance (distance from the

centre of the circular sample). This non-linear trend can be attributed to the temperature gradient that is present across the sample during sample growth. Higher temperatures towards

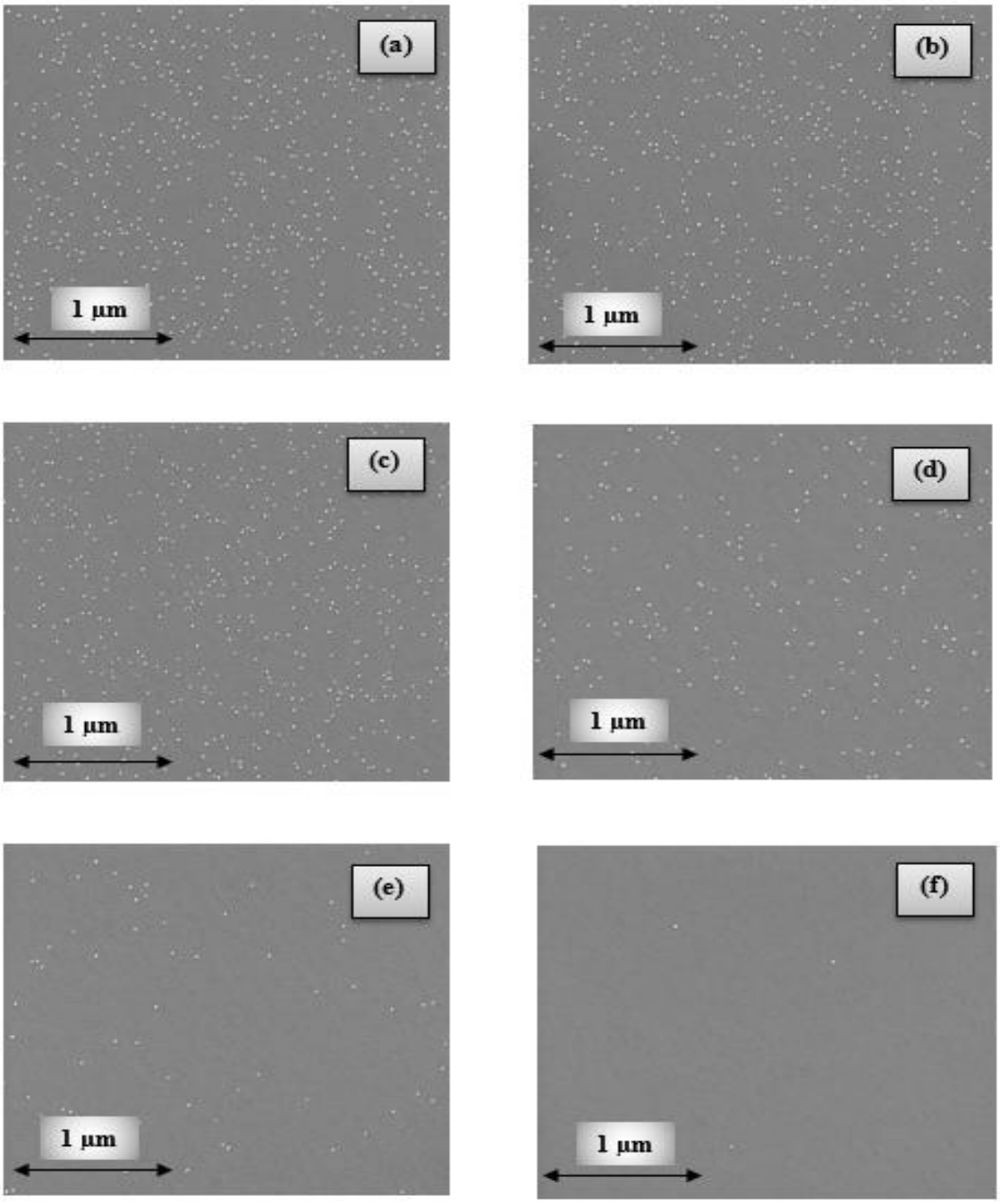

Figure 4.2. Pictures (a) to (f) represent SEM images taken at 2.5 mm intervals starting from the centre and moving towards the sample edge. A non-linear decrease in the QD density is obvious from this set of images.

the edges of the sample result in more evaporation of InAs. In atoms diffuse to energetically favourable positions (away from the apex of the QDs). Thus, there is a low probability of QD formation towards the sample edges. In the central region of the sample, there is a higher density of QDs due to lower substrate temperature. As we move from the centre to the edge, a stark variation in QD density along the radial direction is evident from figure 4.2.

4.2 Results from AFM

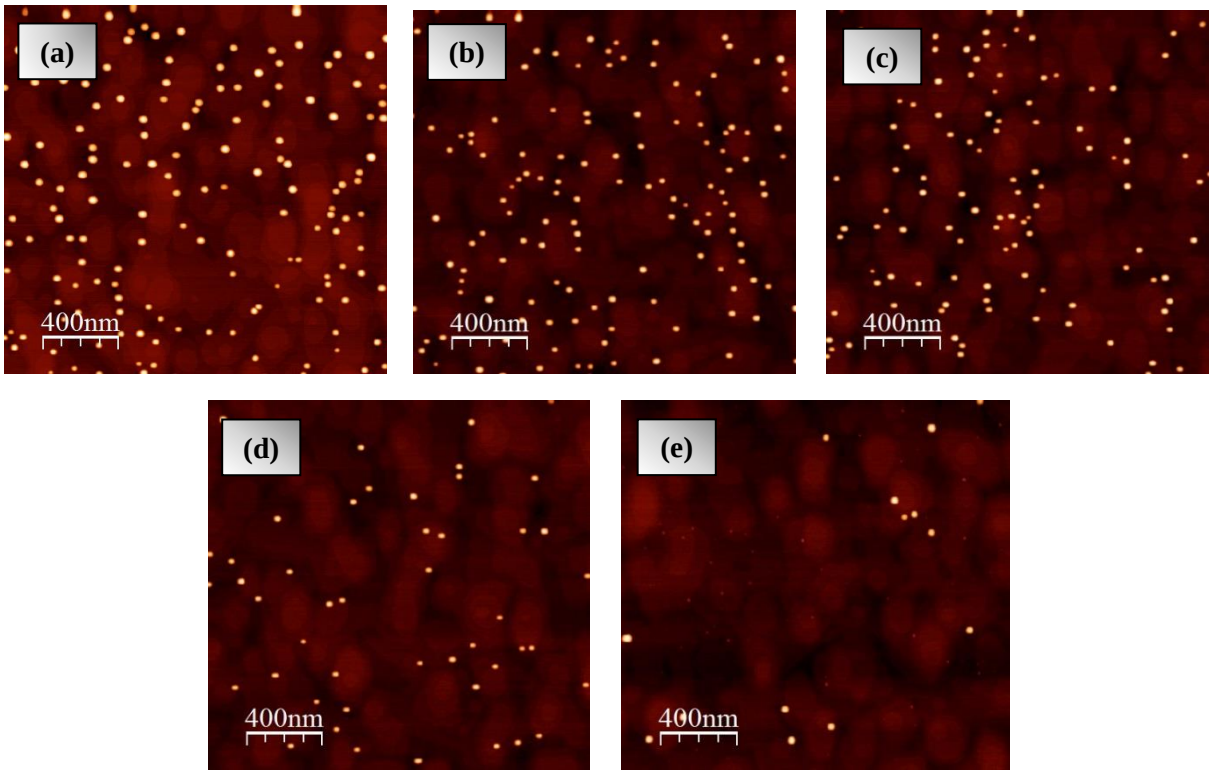

Figure 4.3. Pictures (a) to (e) are AFM images taken at 2.5 mm intervals starting from the centre and moving towards the sample edge. The small, bright yellow structures are surface QDs. Larger, darker shapes in the background are the nucleation sites of embedded QDs. Surface morphology properties of QDs are obtained from these images. It is noted that there is a decrease in QD density as we move from the centre towards the sample edge.

AFM measurements are performed on the samples containing surface QDs. As in the case of SEM imaging, the samples are studied in intervals of 2.5 mm moving from the centre towards the sample edge. AFM measurements provide information about how QD height varies across the sample. Figure 4.4 shows a plot that displays variation in QD height with respect to radial distance. It is noted that there is negligible difference in average height of the QDs, with the average QD height being around 15 nm across the sample.

The purpose of performing AFM measurements is to determine the structural properties of the QDs embedded in the GaAs matrix through the information obtained from studying the surface QDs. However, due to GaAs capping over the embedded QDs, there is a slight reduction in QD height. This reduction is not evident in the case of surface QDs because there is no capping layer. Hence, it is not prudent to conclude the heights of embedded QDs from the AFM measurements. The AFM measurements nevertheless provide useful feedback while growing the samples regarding the formation and structure of QDs, and therefore help to plan the growth of subsequent samples.

Table 4.2. Radial distance vs Average QD height.

Distance from centre of the sample (mm)	Average QD height
0	15.1 +/- 0.8
2.5	15.8 +/- 0.8
5	15.5 +/- 0.8
7.5	15.9 +/- 0.8
10	15.3 +/- 0.8

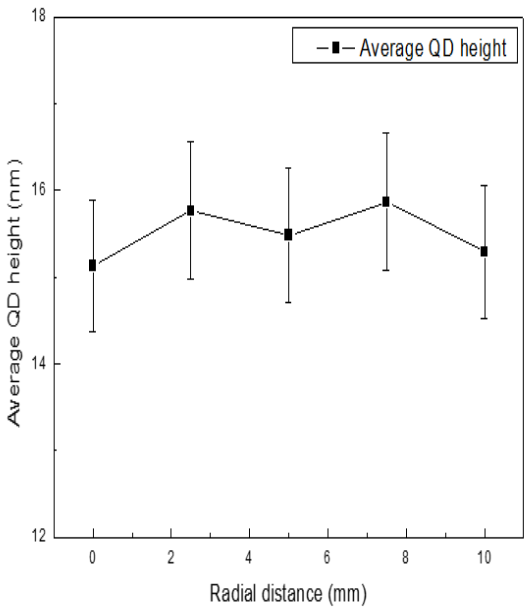

Figure 4.4. Plot showing variation in QD height with respect to radial distance.

An interesting observation made from the AFM images in figure 4.3 is the lateral positioning of surface QDs. From a magnified view of the images, it is noted that surface QDs generally tend to grow on the outer regions of embedded QDs' nucleation sites. It is not relevant to the results presented in this thesis, but it is interesting to learn how QD growth is affected by the topography of embedded structures.

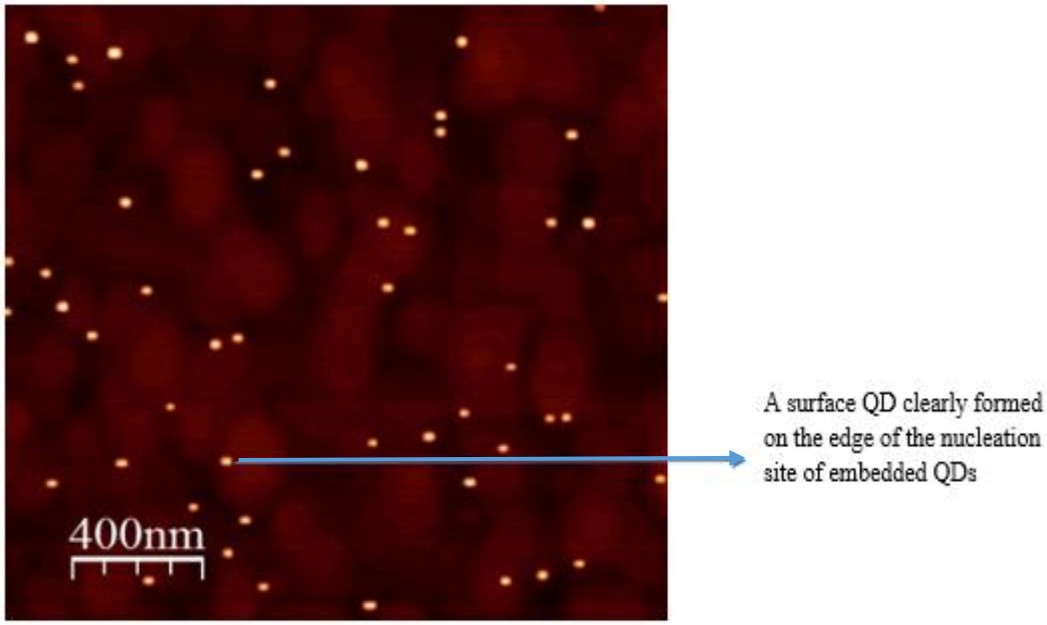

Figure 4.5. An observation of the lateral positioning of surface QDs. Bright, yellow structures are surface QDs, while the faded, dark-red structures are the nucleation sites of embedded QDs.

4.3 Results from low temperature PL

LTPL measurements are performed for samples that contain embedded QDs under the GaAs capping layer. Important optical properties including InAs QD peak wavelength and InAs WL peak wavelength are measured. Table 4.3 displays the results from LTPL experiments. The peak emission wavelength from the WL at different areas across the sample remains relatively constant, as expected. The peak emission wavelength from the QDs reduces non-linearly due

to reduction in QD size on outer regions of the sample. Reduction in physical size of the QDs leads to a higher emission energy [61], [62]. The reduction in size can also be partially attributed to higher growth temperatures towards the sample edge leading to more intermixing between GaAs matrix and the InAs QD layer. The intermixing changes the chemical composition of InAs QDs (with more Ga present in the QDs) and results in changes in the energy structure. By referring to figure 2.6, the bandgap can be theoretically determined for different compositions of In, Ga and As.

Table 4.3. PL data collected from samples with surface InAS QDs on top of 100 nm GaAs capping layer, under which there is a layer of embedded InAs QDs (refer figure 3.3). PL intensity from embedded QDs decreases as we move away from the sample center. This evidence is confirmed by a subsequent increase in PL intensity from the wetting layer (due to the lack of QDs). A blue-shift in wavelength is also seen from the results of this experiment. This shortening of wavelength of QDs is attributed to the QDs becoming smaller towards the sample edge.

Distance from center of the sample (mm)	**Peak emission wavelength from InAs wetting layer (nm)**	**Peak emission wavelength from InAs QDs (nm)**	**Peak emission intensity from InAs wetting layer (a.u.)**	**Peak emission intensity from embedded InAs QDs (a.u.)**
1.65	862	962	2.26×10^{-5}	2.33×10^{-3}
4.65	863	947	4.17×10^{-5}	2.69×10^{-3}
7.4	864	940	8.11×10^{-5}	2.28×10^{-3}
10.2	864	929	4.34×10^{-5}	1.99×10^{-3}
13	864	926	1.56×10^{-5}	6.55×10^{-4}

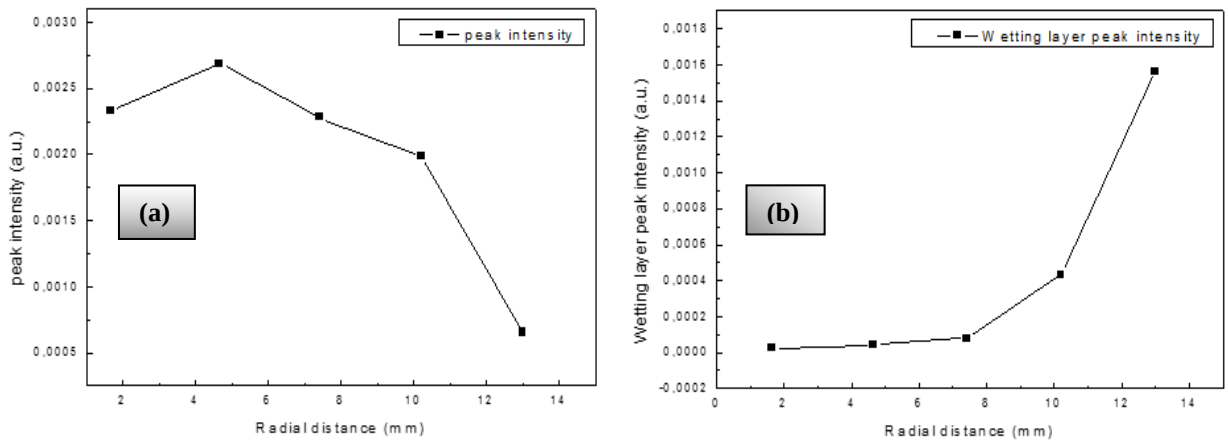

Figure 4.6. (a) QD peak intensity vs radial distance **(b)** WL peak intensity vs radial distance

Figures 4.6 (a) and (b) depict the variation in PL intensity from the WL and the QDs, respectively, across the sample when moving away from the centre. As the density of QDs decreases across the radius of the sample, the number of available QDs for carriers to relax in also decreases. Therefore, the carriers end up spending more time in the WL and recombine eventually. Hence, there is lower PL emission intensity from the WL in areas with high QD density, whereas, PL response from WL dominates towards the sample edge (areas with low QD density). This scenario is quite clear from figure 4.7, where, in the absence of a QD to relax into, the charge carriers would simply stay in the WL.

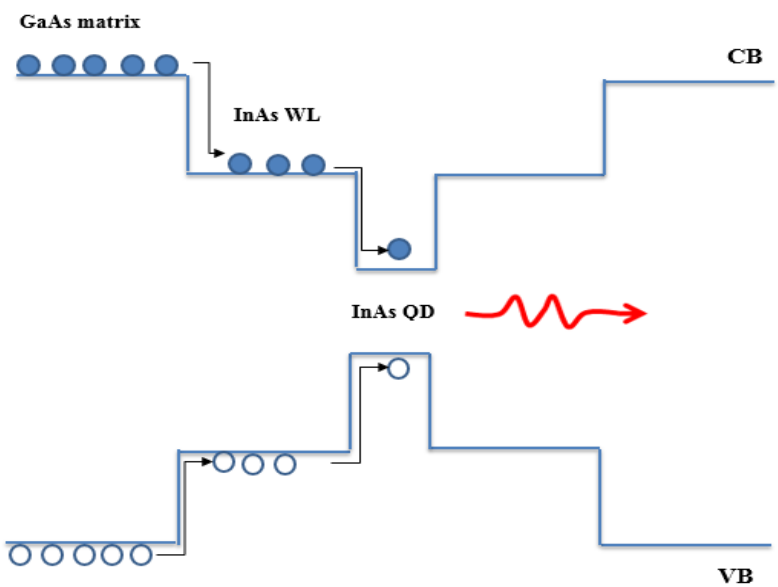

Figure 4.7. A schematic illustration of the relaxation and recombination processes in the InAs/GaAs QD system.

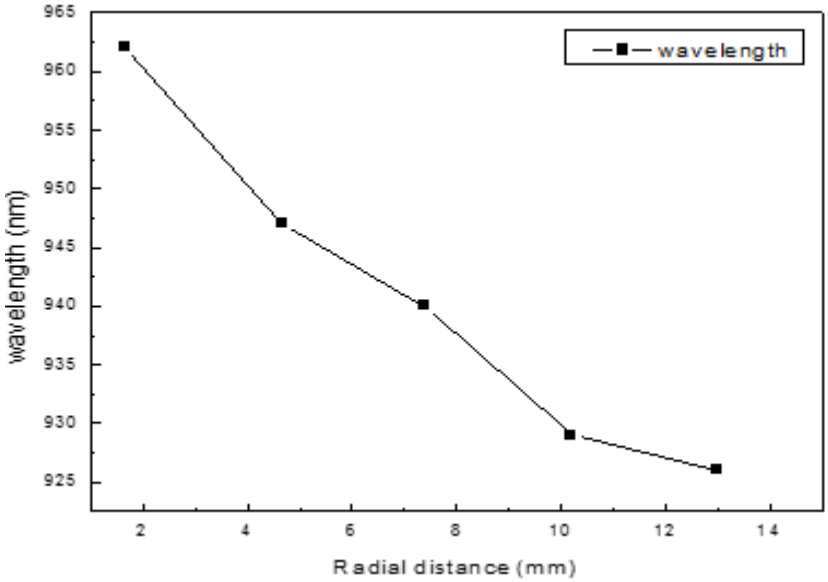

Figure 4.8. Peak QD emission wavelength vs distance from centre of the sample.

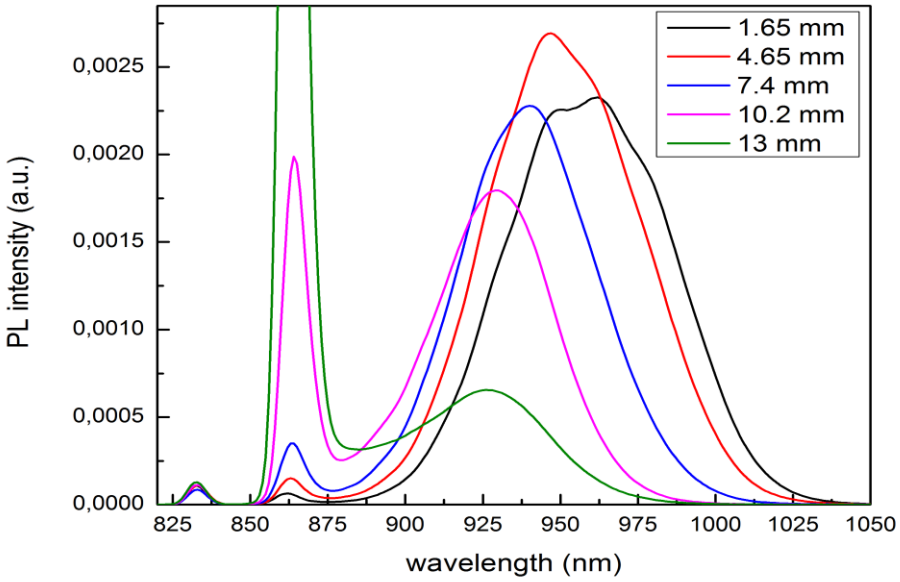

Figure 4.9. Spectra from QDs at different radial distances with 500 µW excitation power.

The reason for the formation of smaller QDs towards the sample edge is due to the temperature gradient present during sample growth (see section 3.1). This results in more In atoms to diffuse across the surface, thus reducing the In content (with consequently more Ga composition in the QDs due to intermixing of layers). Therefore, the combination of variation in structural

properties and chemical composition of the QDs across the sample causes the emission wavelength to decrease (as shown in figures 4.8 and 4.9). A decrease of In content in the QDs also leads the peak PL emission to shift to shorter wavelengths. The energy structure changes due to variation in the III-V material's chemical composition (in this case InAs). The bandgap becomes smaller, leading to PL emission of higher energy (thus, shorter wavelength). Figure 4.8 is a plot that shows decreasing PL emission wavelength while moving towards the sample edge.

4.4 Results from μ-PL

In the μ-PL spectroscopy experiments performed during this thesis, individual QDs from different samples that have varying GaAs cap layer thicknesses were studied. From the

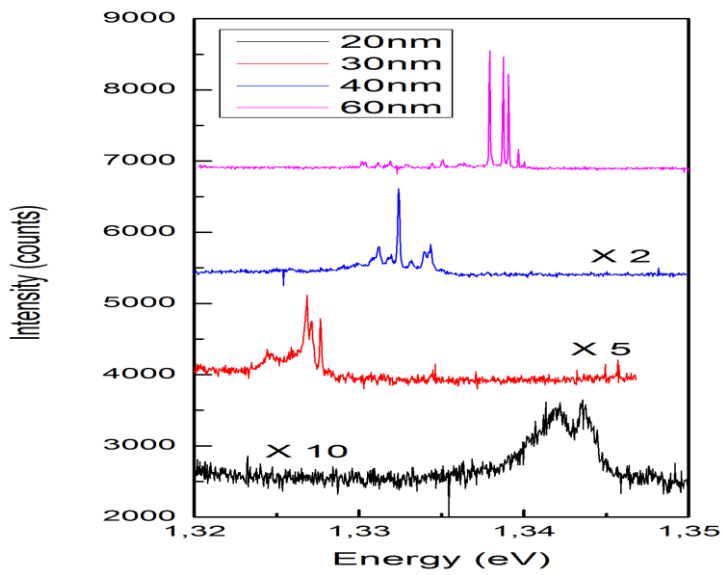

Figure 4.10. Plot of PL spectra from individual QDs in samples with different cap thickness.

results, it is evident that as the QDs get closer to the surface, their PL linewidths become wider. This is due to the close proximity to GaAs surface states that provide the charge carriers with

direct pathways to non-radiative recombination. Figure 4.10 shows a plot of the spectra from individual QDs in samples with different GaAs cap layer thicknesses.

An important characteristic of PL spectra from QDs are excitonic linewidths. The samples of varying capping layer thicknesses are excited with different laser excitation powers in order to resonantly excite the embedded InAs QDs, GaAs matrix and the InAs WL separately. Exciting each layer separately affects the type of excitons formed and their corresponding intensities. Figures 4.11, 4.12 and 4.13 show power-dependent PL spectra from the sample with 60 nm cap layer for different excitation energies.

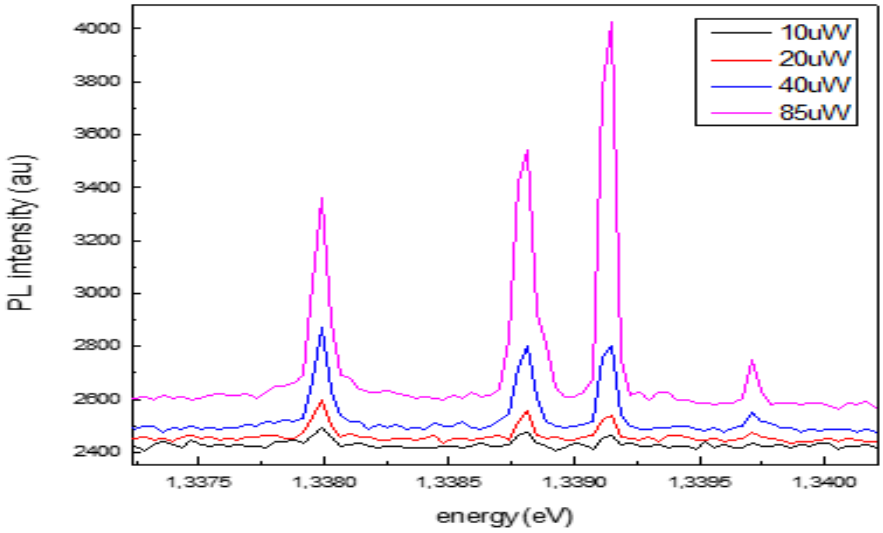

Figure 4.11. Power-dependent PL spectra from 895 nm laser excitation

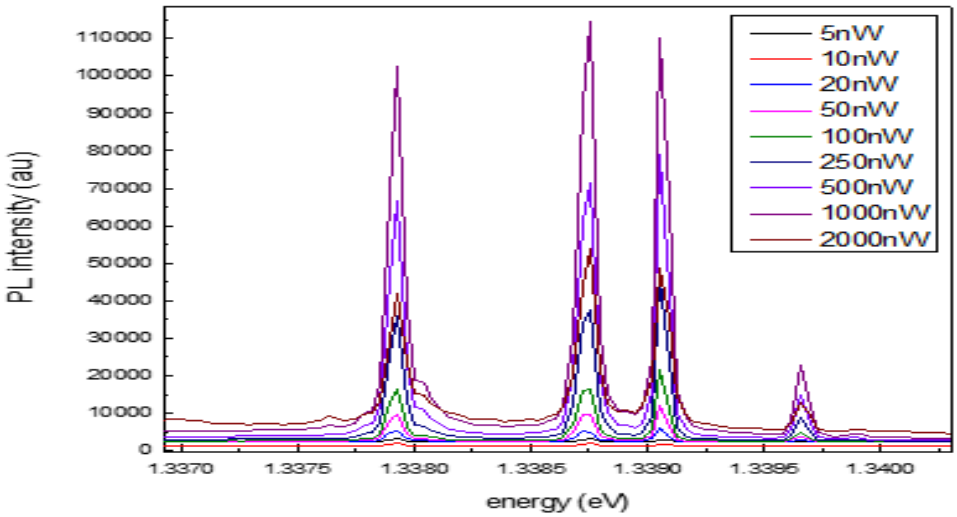

Figure 4.12. Power-dependent PL spectra from 850 nm laser excitation

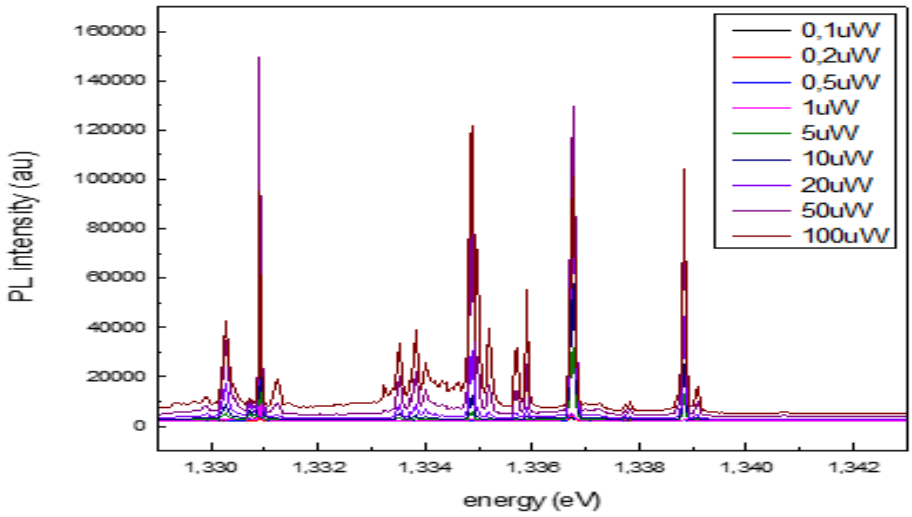

Figure 4.13. Power-dependent PL spectra from 640 nm laser excitation

Three separate lasers of 895 nm, 850 nm and 640 nm are used for resonantly exciting the InAs QDs, InAs WL and GaAs matrix separately. It is evident from the results that the excitonic peaks shift based on which part of the sample is excited resonantly.

4.5 Results from time-resolved photoluminescence (TRPL) spectroscopy

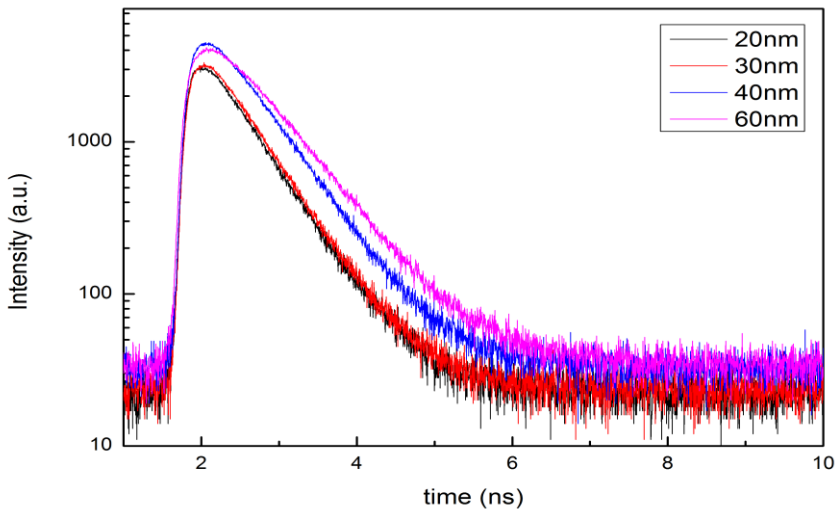

Figure 4.14. Time traces for QDs that are at 20 nm, 30 nm, 40 nm and 60 nm from the sample surface.

The results from TRPL spectroscopy are presented in this section. The samples were excited with two different excitation lasers of 640 nm and 850 nm with a periodic pulse repetition rate of 80 MHz. In figure 4.13, the time traces for samples with capping layer thicknesses of 20 nm, 30 nm, 40 nm and 60 nm are presented in a single plot. The incident power of the focused laser spot on the sample was 1 µW. It can be seen from figure 4.14 that the lifetimes of the carriers

are shorter when the QDs are closer to the sample surface. QDs that are situated at distances of 20 nm and 30 nm from the surface exhibit very similar carrier lifetimes while those situated further away (40 nm and 60 nm) demonstrate a significant increase in their carriers' lifetimes.

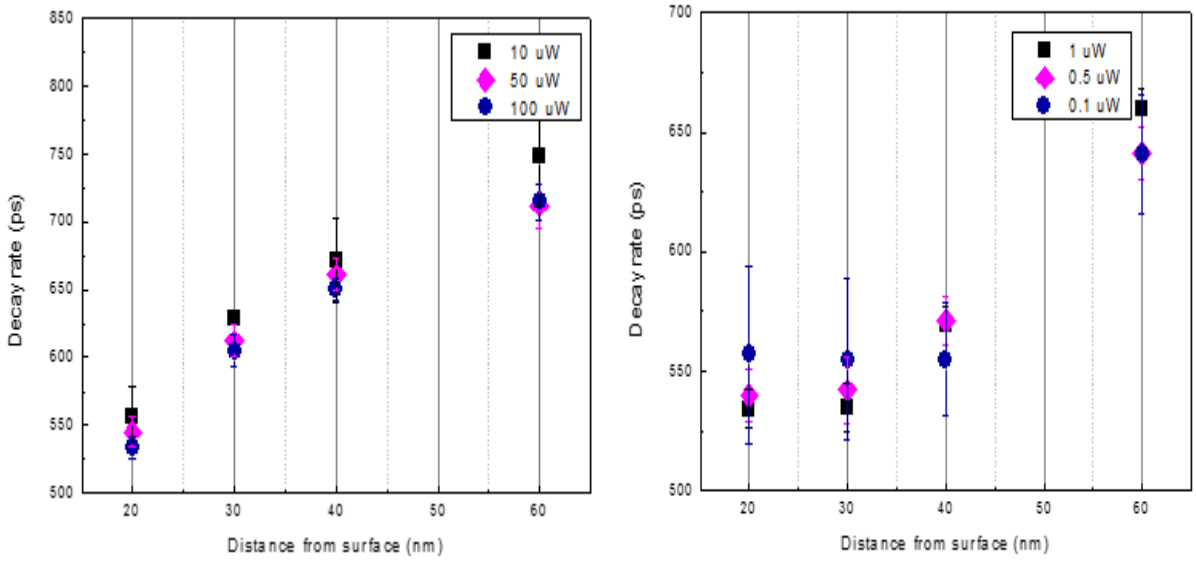

Figure 4.15. Decay rates for QDs excited by 850 nm (left) and 640 nm (right) lasers.

The decay rates for the carrier lifetimes are presented in figure 4.15. Excitation wavelengths of 640 nm and 850 nm were used in a power dependent excitation scheme. The decay rates decrease for QDs that are close to the surface, resulting in very short-lived charge carriers. The proximity of the surface creates possible pathways for carriers to recombine immediately to surface states nonradiatively. This is more prominenent as the QDs get closer to the surface.

Chapter 5

5 Conclusions

In this thesis, the optical properties of close-to-surface InAs/GaAs quantum dots have been studied using μ-PL spectroscopy and time-resolved PL spectroscopy. From the μ-PL spectroscopy results, it is evident that for QDs closer to the surface, their PL linewidths are broader. This could be due to interactions of the QDs with the surface. Two possible mechanisms that could be responsible for this phenomenon are dephasing and spectral diffusion. Though the nature of surface states is not very clear, it is safe to assume that some carriers are trapped by these states and they generate an electric field that randomly shifts the emission wavelengths of QDs situated nearby. If the trapping processes are slower than the spontaneous emission lifetime of the QDs, spectral diffusion occurs. In this case, the QDs would experience a static electric field each time they spontaneously emit a photon. These photons would have slightly different energies with broader linewidths and would form an inhomogenously broadened emission spectrum. Conversely, if the trapping lifetimes were faster when compared to the spontaneous emission lifetimes of the QDs, all emitted photons would have the same energy with a broadened linewidth, which is due to dephasing of the electronic coherence between states in the conduction and valence bands. Since the PL spectra don't show any distinction qualitatively, it is not possible to distinguish between dephasing and spectral diffusion mechanisms.

In summary, individual InAs QDs at close proximities to the surface were grown and studied systematically. The distance between the WL and surface was controllably varied from 20 nm to 60 nm and the corresponding photoluminescence intensity, wavelength, linewidth and lifetime were observed. For single QDs situated within 20 nm to 40 nm from the surface, broadened emission linewidths were observed. QDs closer to the surface also exhibit shorter carrier lifetimes, most likely due to the availability of nonradiative pathways provided by the proximal surface states.

BIBLIOGRAPHY

[1] A. El Fatimy *et al.*, “Ultra-broadband photodetectors based on epitaxial graphene quantum dots”, *Nanophotonics*, vol. 7, no. 4, pp. 735–740, Mar. 2018.

[2] M. K. Choi, J. Yang, T. Hyeon, and D.-H. Kim, “Flexible quantum dot light-emitting diodes for next-generation displays”, *npj Flex. Electron.*, vol. 2, no. 1, p. 10, Dec. 2018.

[3] H. Liu *et al.*, “Long-wavelength InAs/GaAs quantum-dot laser diode monolithically grown on Ge substrate”, *Nat. Photonics*, vol. 5, no. 7, pp. 416–419, Jul. 2011.

[4] Z. Zheng, H. Ji, P. Yu, and Z. Wang, “Recent Progress Towards Quantum Dot Solar Cells with Enhanced Optical Absorption”, *Nanoscale Res. Lett.*, vol. 11, no. 1, p. 266, Dec. 2016.

[5] P. Yu, J. Wu, L. Gao, H. Liu, and Z. Wang, “InGaAs and GaAs quantum dot solar cells grown by droplet epitaxy”, *Sol. Energy Mater. Sol. Cells*, vol. 161, pp. 377–381, Mar. 2017.

[6] M. Schiavon, G. Vallone, F. Ticozzi, and P. Villoresi, “Heralded single-photon sources for quantum-key-distribution applications”, *Phys. Rev. A*, vol. 93, no. 1, p. 012331, Jan. 2016.

[7] A. Fiore *et al.*, “Telecom-wavelength single-photon sources for quantum communications”, *J. Phys. Condens. Matter*, vol. 19, no. 22, p. 225005, Jun. 2007.

[8] M. D. Eisaman, J. Fan, A. Migdall, and S. V. Polyakov, “Invited Review Article: Single-photon sources and detectors”, *Rev. Sci. Instrum.*, vol. 82, no. 7, p. 071101, Jul. 2011.

[9] T. Yamaguchi *et al.*, “Single-photon emission from single quantum dots in a hybrid pillar microcavity”, *Appl. Phys. Lett.*, vol. 92, no. 8, pp. 1–4, 2008.

[10] E. Moreau, I. Robert, L. Manin, V. Thierry-Mieg, J. M. Gérard, and I. Abram, “Quantum cascade of photons in semiconductor quantum dots”, *Phys. Rev. Lett.*, vol. 87, no. 18, pp. 183601-1-183601–4, 2001.

[11] V. Zwiller *et al.*, “Single quantum dots emit single photons at a time: Antibunching

experiments", *Appl. Phys. Lett.*, vol. 78, no. 17, pp. 2476–2478, 2001.

[12] C. Santori, M. Pelton, G. Solomon, Y. Dale, and Y. Yamamoto, "Triggered single photons from a quantum dot", *Tech. Dig. - Summ. Pap. Present. Quantum Electron. Laser Sci. Conf. QELS 2001*, no. c, p. 186, 2001.

[13] Z. Yuan *et al.*, "Electrically driven single-photon source.", *Science*, vol. 295, no. 5552, pp. 102–5, 2002.

[14] P. Senellart, G. Solomon, and A. White, "High-performance semiconductor quantum-dot single-photon sources", *Nat. Nanotechnol.*, vol. 12, no. 11, pp. 1026–1039, Nov. 2017.

[15] J.-Y. Marzin, J.-M. Gérard, A. Izraël, D. Barrier, and G. Bastard, "Photoluminescence of Single InAs Quantum Dots Obtained by Self-Organized Growth on GaAs", *Phys. Rev. Lett.*, vol. 73, no. 5, pp. 716–719, Aug. 1994.

[16] L. Landin, M. S. Miller, M.-E. Pistol, C. E. Pryor, and L. Samuelson, "Optical studies of individual InAs quantum dots in GaAs: few-particle effects", *Science*, vol. 280, no. 5361, pp. 262–4, Apr. 1998.

[17] E. Dekel, D. Gershoni, E. Ehrenfreund, J. M. Garcia, and P. M. Petroff, "Carrier-carrier correlations in an optically excited single semiconductor quantum dot", *Phys. Rev. B*, vol. 61, no. 16, pp. 11009–11020, Apr. 2000.

[18] P. Michler, A. Kiraz, L. Zhang, C. Becher, E. Hu, and A. Imamoglu, "Laser emission from quantum dots in microdisk structures", *Appl. Phys. Lett.*, vol. 77, no. 2, p. 184, Jun. 2000.

[19] P. Michler *et al.*, "A quantum dot single-photon turnstile device.", *Science*, vol. 290, no. 5500, pp. 2282–5, Dec. 2000.

[20] J. Vučković and Y. Yamamoto, "Photonic crystal microcavities for cavity quantum electrodynamics with a single quantum dot", *Appl. Phys. Lett.*, vol. 82, no. 15, pp. 2374–2376, Apr. 2003.

[21] K. Hennessy *et al.*, "Square-lattice photonic crystal microcavities for coupling to single InAs quantum dots", *Appl. Phys. Lett.*, vol. 83, no. 18, pp. 3650–3652, Nov. 2003.

[22] A. Y. Cho and J. R. Arthur, “Molecular beam epitaxy”, *Prog. Solid State Chem.*, vol. 10, no. PART 3, pp. 157–191, Jan. 1975.

[23] M. A. Herman and H. Sitter, *Molecular Beam Epitaxy*, vol. 7. 1996.

[24] Y. Horikoshi and M. Kawashima, “Growth Mechanism of GaAs during Migration-Enhanced Epitaxy at Low Growth Temperatures”, *Jpn. J. Appl. Phys.*, vol. 28, no. Part 1, No. 2, pp. 200–209, Feb. 1989.

[25] S. Franchi, *Molecular Beam Epitaxy: Fundamentals, Historical Background and Future Prospects*. 2013.

[26] B. R. Pamplin, *Molecular beam epitaxy*. Pergamon Press, 1980.

[27] E. H. C. Parker, *The Technology and physics of molecular beam epitaxy*. Plenum Press, 1985.

[28] T. Sakamoto, N. J. Kawai, T. Nakagawa, K. Ohta, and T. Kojima, “Intensity oscillations of reflection high- energy electron diffraction during silicon molecular beam epitaxial growth”, *Appl. Phys. Lett.*, vol. 47, no. 6, pp. 617–619, Sep. 1985.

[29] S. A. Chambers, T. T. Tran, and T. A. Hileman, “Auger electron spectroscopy as a real-time compositional probe in molecular beam epitaxy”, *J. Vac. Sci. Technol. A Vacuum, Surfaces, Film.*, vol. 13, no. 1, pp. 83–91, Jan. 1995.

[30] J.-F. Jia, X. Ma, X. Chen, T. Sakurai, and Q.-K. Xue, “STM and MBE: one of the best combinations”, *J. Phys. D. Appl. Phys.*, vol. 44, no. 46, p. 464007, Nov. 2011.

[31] S. Tsukamoto, G. R. Bell, and Y. Arakawa, “In-situ scanning tunneling microscopy observation of InAs quantum dots on GaAs[001] during molecular beam epitaxy growth”, in *16th IPRM. 2004 International Conference on Indium Phosphide and Related Materials, 2004.*, pp. 68–73.

[32] J. E. Ayers, T. Kujofsa, P. Rango, and J. E. Raphael, *Heteroepitaxy of semiconductors : theory, growth, and characterization*. .

[33] T. Hakkarainen, “Site-Controlled Epitaxy and Fundamental Properties of InAs Quantum Dot Chains”, *... Tek. yliopisto. Julk. Univ. ...*, 2014.

[34] J. W. Matthews and A. E. Blakeslee, “Defects in epitaxial multilayers: I. Misfit

dislocations", *J. Cryst. Growth*, vol. 27, pp. 118–125, Dec. 1974.

[35] X. Wallart, O. Schuler, D. Deresmes, and F. Mollot, "Composition effect on the growth mode, strain relaxation, and critical thickness of tensile Ga1−xInxP layers", *Appl. Phys. Lett.*, vol. 76, no. 15, p. 2080, Apr. 2000.

[36] I. N. Stranski and L. Krastanow, "Zur Theorie der orientierten Ausscheidung von Ionenkristallen aufeinander", *Monatshefte für Chemie*, vol. 71, no. 1, pp. 351–364, Dec. 1937.

[37] L. Goldstein, F. Glas, J. Y. Marzin, M. N. Charasse, and G. Le Roux, "Growth by molecular beam epitaxy and characterization of InAs/GaAs strained-layer superlattices", *Appl. Phys. Lett.*, vol. 47, no. 10, pp. 1099–1101, Nov. 1985.

[38] A. Madhukar, Q. Xie, P. Chen, and A. Konkar, "Nature of strained InAs three-dimensional island formation and distribution on GaAs(100)", *Appl. Phys. Lett.*, vol. 64, no. 20, pp. 2727–2729, May 1994.

[39] J. M. Moison, F. Houzay, F. Barthe, L. Leprince, E. André, and O. Vatel, "Self-organized growth of regular nanometer-scale InAs dots on GaAs", *Appl. Phys. Lett.*, vol. 64, no. 2, pp. 196–198, Jan. 1994.

[40] D. Heitmann, *Quantum materials, lateral semiconductor nanostructures, hybrid systems and nanocrystals*. Springer, 2010.

[41] K. H. Schmidt, G. Medeiros-Ribeiro, U. Kunze, G. Abstreiter, M. Hagn, and P. M. Petroff, "Size distribution of coherently strained InAs quantum dots", *J. Appl. Phys.*, vol. 84, no. 8, p. 4268, Oct. 1998.

[42] H. . Liu *et al.*, "Size and shape evolution of self-assembled coherent InAs/GaAs quantum dots influenced by seed layer", *J. Cryst. Growth*, vol. 227–228, pp. 1005–1009, Jul. 2001.

[43] N. N. Ledentsov *et al.*, "Direct formation of vertically coupled quantum dots in Stranski-Krastanow growth", *Phys. Rev. B*, vol. 54, no. 12, pp. 8743–8750, Sep. 1996.

[44] P. Yu *et al.*, "Optical anisotropy in vertically coupled quantum dots", *Phys. Rev. B*, vol. 60, no. 24, pp. 16680–16685, Dec. 1999.

[45] P. B. Joyce, T. J. Krzyzewski, G. R. Bell, B. A. Joyce, and T. S. Jones, “Composition of InAs quantum dots on GaAs(001): Direct evidence for (In,Ga)As alloying”, *Phys. Rev. B*, vol. 58, no. 24, pp. R15981–R15984, Dec. 1998.

[46] C. Heyn, A. Bolz, T. Maltezopoulos, R. L. Johnson, and W. Hansen, “Intermixing in self-assembled InAs quantum dot formation”, *J. Cryst. Growth*, vol. 278, no. 1–4, pp. 46–50, May 2005.

[47] J. M. García *et al.*, “Intermixing and shape changes during the formation of InAs self-assembled quantum dots”, *Appl. Phys. Lett.*, vol. 71, no. 14, p. 2014, Aug. 1998.

[48] Jose Maria Roman, “State-of-the-art of III-V solar cell fabrication technologies, device designs and applications”, *Adv. Photovolt. Cell Des.*, 2004.

[49] Juha Tommila, *Nanoscale architecture for site-controlled epitaxy and antireflective coatings*. 2013.

[50] J. P. van der Ziel, R. Dingle, R. C. Miller, W. Wiegmann, and W. A. Nordland, “Laser oscillation from quantum states in very thin GaAs−Al $_{0.2}$ Ga $_{0.8}$ As multilayer structures”, *Appl. Phys. Lett.*, vol. 26, no. 8, pp. 463–465, Apr. 1975.

[51] M. Henini, *Handbook of self assembled semiconductor nanostructures for novel devices in photonics and electronics*. Elsevier, 2008.

[52] P. Michler, *Single semiconductor quantum dots*. Springer, 2008.

[53] N. Tang, “Effect of size non-uniformity on photoluminescence from ensembles of InAs quantum dots embedded in GaAs”, *J. Mater. Sci.*, vol. 42, no. 16, pp. 6913–6916, Jun. 2007.

[54] M. Carter, J. C. Shieh, N. Farra, and G. Harris, *Guide to research techniques in neuroscience*. Mar. 2015.

[55] Z. Liu *et al.*, “A review of fine structures of nanoporous materials as evidenced by microscopic methods”, *Microscopy*, vol. 62, no. 1, pp. 109–146, Feb. 2013.

[56] M. Anderson *et al.*, “An appraisal of high-resolution scanning electron microscopy applied to porous materials”, *JEOL News*, vol. 44, pp. 17–22, Apr. 2009.

[57] M. Suga *et al.*, “Recent progress in scanning electron microscopy for the

characterization of fine structural details of nano materials", *Prog. Solid State Chem.*, vol. 42, no. 1–2, pp. 1–21, May 2014.

[58] I. Horcas, R. Fernández, J. M. Gómez-Rodríguez, J. Colchero, J. Gómez-Herrero, and A. M. Baro, "WSXM : A software for scanning probe microscopy and a tool for nanotechnology", *Rev. Sci. Instrum.*, vol. 78, no. 1, p. 013705, Jan. 2007.

[59] A. M. Stoneham, "Non-radiative transitions in semiconductors", *Reports Prog. Phys.*, vol. 44, no. 12, pp. 1251–1295, Dec. 1981.

[60] S.-Y. Joo, H.-S. Park, D. Kim, B.-S. Kim, C. G. Lee, and W.-B. Kim, "An investigation into the effective surface passivation of quantum dots by a photo-assisted chemical method", *AIP Adv.*, vol. 8, no. 1, p. 015017, Jan. 2018.

[61] A. M. Smith and S. Nie, "Semiconductor nanocrystals: structure, properties, and band gap engineering.", *Acc. Chem. Res.*, vol. 43, no. 2, pp. 190–200, Feb. 2010.

[62] G. Zhong-sheng, W. Hai-long, N. Dong, and F. Song-lin, "Photoluminescence study of InAs/GaAs self-organized quantum dots with bimodal size distribution", *Chinese Phys.*, vol. 9, no. 5, pp. 384–388, May 2000.